J. Fluid Mech. (2012), *vol.* 711, *pp.* 61–100.
doi:10.1017/jfm.2012.369

Three-dimensional instabilities in tornado-like vortices with secondary circulations

David S. Nolan†

Rosenstiel School of Marine and Atmospheric Science, University of Miami, Miami, FL, USA

(Received 12 January 2012; revised 21 May 2012; accepted 17 July 2012;
first published online 19 September 2012)

Tornadoes and other intense atmospheric vortices are known to occasionally transition to a flow structure with multiple vortices within their larger circulations. This phenomenon has long been ascribed to fluid dynamical instability of the inner-core circulation, and many previous studies have diagnosed low-wavenumber unstable modes in tornado-like vortices that resemble the observed structures. However, relatively few of these studies have incorporated the strong vertical motions of the inner-core circulation into the stability analysis, and no stability analyses have been performed using a complete, frictionally driven secondary circulation with strong radial inflow near the surface. Stability analyses are presented using the complete circulations generated from idealized simulations of tornado-like vortices. Fast-growing unstable modes are found that are consistent with the asymmetric structures present in these simulations. Attempts to correlate the structures and locations of these modes with instability conditions for vortices with axial jets derived by Howard & Gupta and by Leibovich & Stewartson produce only mixed results. Analyses of perturbation energy growth show that interactions between eddy fluxes and the radial shear of the azimuthal wind contribute very little to the growth of the dominant modes. Rather, the radial shear of the vertical wind and the vertical shear of the vertical wind (corresponding to deformation in the axial direction) are the primary energy sources for perturbation growth. Relatively weak axisymmetric instabilities are also identified that have some similarity to symmetric oscillations that have been observed in tornadoes.

Key words: vortex breakdown, vortex dynamics, vortex instability

1. Introduction

The tornado is a naturally occurring example of a columnar vortex with strong axial and azimuthal flow. Other phenomena which are conceptually and dynamically similar to tornadoes are waterspouts (weaker, narrower vortices that occur over the ocean), dust devils (smaller and weaker vortices generated in dry convective boundary layers over land), and vortices generated in laboratory experiments and in numerical simulations. In each case the vortex is first formed by forced convergence of a larger-scale rotating flow near a lower boundary. Frictional retardation of the swirling flow adjacent to the lower boundary leads to a stronger, low-level radial inflow which causes the low-level circulation to contract even further, and as a result the peak

† Present address: RSMAS/MPO, 4600 Rickenbacker Causeway, Miami, FL 33149, USA. Email address for correspondence: dnolan@rsmas.miami.edu

azimuthal velocities are achieved at small radius at the top of this frictional boundary layer (Rotunno 1979; Howells, Rotunno & Smith 1988; Fiedler 1993; Lewellen & Lewellen 2007*a*). This intensification process is also known as 'vortex collapse' (Shtern & Hussain 1999; Lewellen & Lewellen 2007*b*).

The boundary layer fluid that converges toward the centre axis must turn upward and in doing so it generates a strong axial (upward) flow along the inside edge of the annulus of peak azimuthal winds. As a result the tornado is similar to vortices that have been studied extensively in the context of the vortex breakdown phenomenon (Hall 1972; Leibovich 1984). Laboratory models of tornadoes can show distinct vortex breakdown structures (Ward 1972; Church *et al.* 1979; Church & Snow 1993). In the atmosphere, the challenges of interpreting fast vortical flow motions by tracking debris and cloud condensate interfaces have made identifying vortex breakdown more difficult. Lugt (1989) provides a discussion and review of observations of tornadoes and waterspouts clearly showing the vortex breakdown structure. However, it is believed that many tornadoes (especially the largest ones) have a 'two-celled' structure with downward flow along the centre axis that reaches the surface. Such a flow would not qualify as a vortex breakdown.

Much as vortex breakdown in the laboratory is often dominated by asymmetries, it is well established from numerous observations that the tornado vortex often 'breaks down' into multiple vortices. These multiple vortices can occur on several scales compared to the tornado itself. Many tornadoes contain within them smaller-scale, transient, 'suction vortices' (Fujita 1970; Agee *et al.* 1977) that evidently contain substantially increased wind speeds relative to the azimuthal-mean wind of the tornado itself. In addition, the tornado vortex sometimes separates into more pronounced, longer-lasting multiple vortices that rotate around each other (Pauley & Snow 1988; Bluestein & Pazmany 2000; Wurman 2002)). In some cases these may become so distinct as to appear as separate, multiple tornadoes embedded within a broader circulation. Laboratory models of tornadoes also show multiple vortices (Ward 1972; Church & Snow 1993) as do numerical simulations (Fiedler 1998; Lewellen, Lewellen & Xia 2000).

The multiple vortex phenomenon has long been ascribed to dynamical instability of the primarily axisymmetric flow of the tornado vortex itself. Early work on vortex stability by Michaelke & Timme (1967) showed that an annulus of elevated vorticity could be unstable to modes with azimuthal wavenumbers n greater than 2. Rotunno (1978) showed that a 'hollow vortex' (zero circulation surrounded by potential flow, equivalent to a cylindrical vortex sheet) could also be unstable to lower wavenumbers ($n = 1$ and $n = 2$) if an axial flow, also discontinuous along the inner-core interface, was added to the basic state. Staley & Gall (1979) performed a numerical stability analysis of an azimuthal wind profile as a function of radius $V(r)$ based on an observed tornado and also found rapidly growing modes with wavenumbers of 2 or greater. Gall (1983) added vertical wind $W(r)$ to the analysis, using $V(r)$ and $W(r)$ obtained from numerical simulations modelled after laboratory experiments that produced tornado-like circulations with multiple vortices. As with Rotunno (1978), Gall (1983) found that adding $W(r)$ caused the unstable modes to assume a spiral structure with the fastest growth occurring for vertical wavelengths that are several times greater than the horizontal wavelengths. The interpretation of Gall (1983) and later Gall (1985) and Steffens (1988) was that the multiple vortex phenomenon results from instability that is primarily due to the radial shear of the azimuthal wind: the primary effect of the radial shear of the vertical wind is to change the structure of

the modes (i.e. spiral versus two-dimensional) rather than to change their fundamental dynamics.

A more complete approach was taken by Walko & Gall (1984, hereafter referred to as WG84). Their basic-state flow was taken from axisymmetric, nonlinear numerical simulations designed after a laboratory model, and the linearized stability analysis was performed for the entire, vertically varying circulation with radial flow $U(r, z)$ as well as $V(r, z)$ and $W(r, z)$. Harmonic variation was presumed only in the azimuthal direction, so that the unstable modes were also allowed to have arbitrary variation in the vertical, i.e. $u'(r, \lambda, z, t) = u_n(r, z) \exp\{in\lambda - i\omega t\}$, where λ is the azimuth angle and ω is the (possibly complex) frequency. The unstable modes were identified by 'growing' disturbances from random initial conditions evolved forward using linearized versions of the model equations. As in previous studies, fast-growing unstable modes were identified with spiral structures that 'tilt back' against the primary circulation, expanding and weakening upward from the surface (excellent illustrations of these modes can be see in figures 6–8 of WG84). The structure and apparent behaviours of these modes were consistent with the multiple vortex phenomenon in observed tornadoes as well as in the contemporary numerical simulations of Rotunno (1984).

However, the numerical simulations used to generate the basic-state vortices of Gall (1983) and WG84 were highly unrealistic in one important aspect: they used a 'free-slip' lower boundary condition. Beginning with the work of Rotunno (1979) and then later by Howells *et al.* (1988) and Fiedler (1993), it has been recognized that a strongly frictional lower boundary condition (either a no-slip condition or a bulk drag-law condition with a significant roughness length) is necessary to generate a realistic tornado-like vortex. Without sufficient surface stress, the radial inflow will be much weaker and the low-level flow will 'separate' from the surface at large radius, generating a broad vortex with nearly stagnant flow and weak downward recirculation along and near the centre axis. Modern large-eddy simulations (Lewellen, Lewellen & Sykes 1997; Lewellen *et al.* 2000) and observations (Bluestein *et al.* 2003; Lee & Wurman 2005), however, support the existence of significant radial inflow at the lowest levels, although not necessarily all the way to the vortex centre. It suffices to say that the frictional boundary layer is an essential component of a realistic tornado-like vortex circulation.

Preliminary work by Nolan & Montgomery (2002*a*) attempted to address this limitation of the aforementioned stability studies. For their basic-state vortex they used time-averaged output from axisymmetric numerical simulations with a no-slip lower boundary condition using the model of Nolan & Farrell (1999*b*, hereafter referred to as NF99*b*). Nolan & Montgomery (2002*a*) did find unstable modes with some similarities to those of WG84 but generally with more complex structures, especially near the surface where there are large variations of U, V and W in height as well as radius. While the NF99*b* basic-state flows were an improvement, they were still not quite appropriate in the following sense: the time mean of an axisymmetric simulation that is unstable to asymmetric disturbances will not be the time mean of an equivalent three-dimensional simulation.

As discussed by Hall & Sardeshmukh (1998), there are advantages and disadvantages to studying the linearized dynamics about each of these two states: the temporal mean of a symmetric model and the azimuthal- and temporal mean of a simulation with eddies. In the former case, the interpretation is very straightforward and the evolution of any small-amplitude perturbation is accurately depicted by linearization about the mean state. However, the symmetric temporal mean may be quite different from the three-dimensional temporal mean (it fact, in may not even be

close to a realizable azimuthal-mean state), so the modes and dynamics identified in this analysis may not be relevant to the eddies that actually occur. While linearization about the azimuthal and temporal mean of a flow with eddies seems more likely to diagnose asymmetric motions that actually occur, such linearization neglects the effects of the full eddy field on small-amplitude perturbations themselves. Most studies presume this effect can be neglected.

In this paper we present fully three-dimensional stability analyses of the azimuthal- and temporal-mean flows of tornado-like vortices generated from the numerical simulations of Fiedler (2009). These simulations are fully three-dimensional and performed with greater resolution and at Reynolds number higher than has been used before for stability analyses. (To be more specific, if we choose the radius of maximum winds as the length scale and the peak wind speed as the velocity scale, then $Re = 22$ for most of the results of Walko & Gall (1984); for Nolan & Montgomery (2002*a*) $Re = 222$; and this study uses vortices with $Re = 125$, 345 and 1500.) An additional basic state is also considered which is the temporal mean of an axisymmetric simulation. Relevant details on the numerical simulations and the four basic-state vortices are presented in § 2. Section 3 describes the linearized equations and the numerical methods for extracting the modes. Section 4 shows results of stability analyses for each vortex and shows the three-dimensional structures of some of these unstable modes. Section 5 analyses the dynamics of the unstable modes, their interactions with the basic state, and their mechanisms for perturbation energy growth. Summary and conclusions are presented in § 6.

2. Basic-state vortices

2.1. *Temporal and azimuthal means of three-dimensional simulations*

For tornado-like vortices we use three of the vortices produced in the idealized, three-dimensional numerical simulations of Fiedler (2009, hereafter referred to as F09). The numerical model used in that study is the same as that described in Fiedler (1998), which extends to three dimensions the modelling strategy used in Fiedler (1993) and Fiedler (1994). In this approach, a tornado-like vortex is generated by imposing a specified vertical forcing function $F_z(r, z)$ at the centre axis of a cylinder (for axisymmetric flow) or a box (for three-dimensional simulations) that is rotating at a constant angular velocity Ω. Upward motion around the centre axis forces low-level convergence that generates a swirling flow in the lower levels of the domain. For certain ranges of Ω and eddy viscosity ν such a flow will contract into a quasi-steady, intense vortex that, despite the simplicity of the model, shows structure and behaviours that are similar to observed tornado wind fields.

The three-dimensional simulations of F09 use a rectangular domain in the range $-2 \leqslant x \leqslant 2$, $-2 \leqslant y \leqslant 2$, $0 \leqslant z \leqslant 1$. The vertical forcing is centred at $x = 0$, $y = 0$ with the form

$$F_z(x, y, z) = 1.262 \exp\{-10(x^2 + y^2) - 20\,(z - 1/2)^2\}. \tag{2.1}$$

The amplitude is chosen so that an undisturbed fluid parcel accelerating upward along the centre axis would reach a velocity of 1.0. This provides the scale of the peak velocities of the simulated vortices (the so-called 'thermodynamic speed limit'; Lilly 1969; Fiedler & Rotunno 1986). All units are non-dimensional. The environmental rotation Ω is incorporated by adding a Coriolis parameter $f = 2\Omega$ to the equations of motion. F09 uses a stretched grid with much larger grid spacing in the upper parts of the domain, thereby requiring increased ν for numerical stability. For this reason, ν

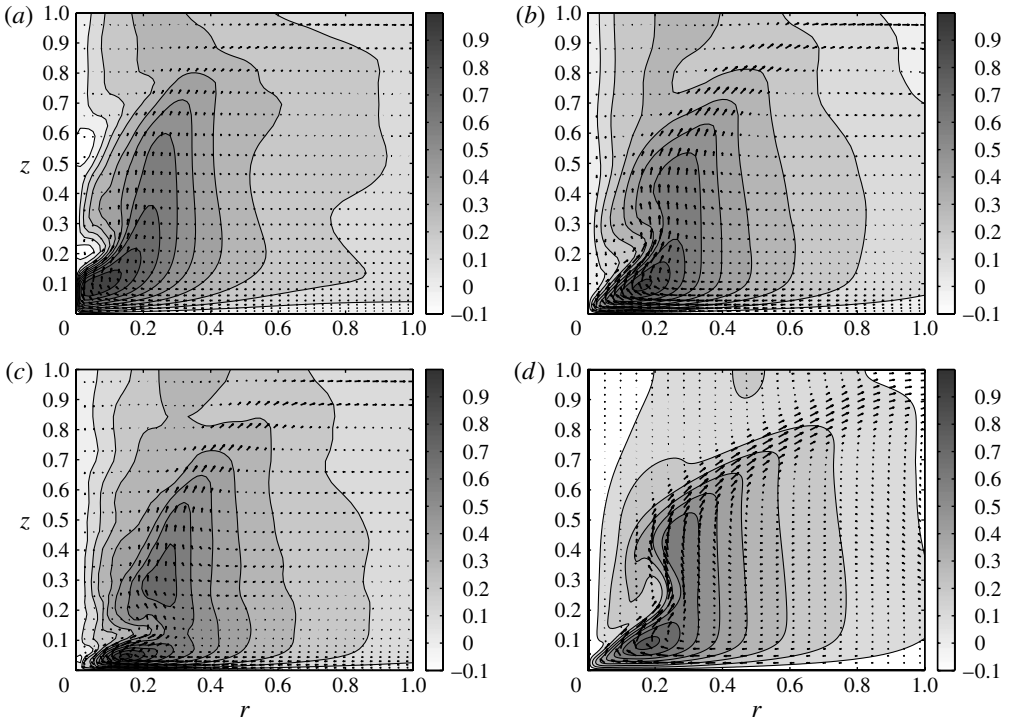

FIGURE 1. Time- and azimuthal-mean flows, V and $[U, W]$, computed from three of the numerical simulations of tornado-like vortices by Fiedler (2009): (*a*) the one-celled vortex (OCV), max $V = 1.00$, min $= -0.64$, interval $= 0.10$, max vector $= 1.64$; (*b*) the drowned vortex jump (DVJ), max $V = 0.92$, min $= -0.10$, interval $= 0.10$, max vector $= 0.64$; (*c*) the two-celled vortex (TCV), max $V = 1.03$, min $= -0.04$, interval $= 0.10$, max vector $= 0.67$; (*d*) the axisymmetric drowned vortex jump (AXI-DVJ), max $V = 0.83$, min $= -0.11$, interval $= 0.10$, max vector $= 0.55$. Meridional flow vectors are plotted at every other grid point from the mean-flow data set, which is equally spaced in the radial direction and stretched in the vertical, except for AXI-DVJ, where the vectors are plotted every sixth point on a grid that is equally spaced in both directions. Only the part of the domain from $r = 0$ to $r = 1$ is shown.

varies with height, ranging from $\nu = 0.001$ in the upper part of the domain to values such as $\nu = 0.0004$ or $\nu = 0.0001$ in the lower part.

As found by NF99*b* and Nolan (2005*b*), the structure of the tornado-like vortex is strongly controlled by a dimensionless parameter often called the vortex Reynolds number $Re_V = \Omega L^2/\nu$, where L is a horizontal length scale of the vertical forcing and ν is the kinematic viscosity; this is equivalent to the rotational Reynolds number $\Omega R^2/\nu$ that controls the flow in rotating-lid experiments of vortex breakdown (Escudier 1984; Serre & Bontoux 2002). For relatively low values of Re_V, the simulated vortex has a steady, columnar appearance near the lower surface that transitions through a vortex breakdown into an unsteady, asymmetric circulation. Such a configuration, where a substantial volume of low-level inflow penetrates toward $r = 0$ and there is a pronounced axial updraft in the low-level core, is often called a 'low-swirl vortex' or a 'one-celled vortex' (hereafter, we use the designation OCV). The simulation of F09 with $f = 0.05$ and $\nu = 0.0004$ at low levels generates an OCV. Averaging the output of this simulation temporally and azimuthally around the centre axis produces the vortex shown in figure 1(*a*). Below $z = 0.2$, the flow is

very steady and the vortex remains nearly fixed at the centre of the computational domain. Above $z = 0.2$, the vortex oscillates with an $n = 1$ asymmetry that spirals backward against the flow with height (turning clockwise upward) as shown in figure 5(*b*) of F09.

As either f is increased or ν is decreased, the boundary layer becomes shallower causing the mass flux of the central updraft to decrease. As a result, the vortex breakdown descends, bringing its central downdraft and localized recirculation towards the surface. The vortex configuration that has this central downdraft just above the vortex surface has been called a 'drowned vortex jump' (hereafter referred to as DVJ: Maxworthy 1973; Snow 1982). F09 generates such a flow with $f = 0.20$ and $\nu = 0.0004$ and its temporal–azimuthal mean is shown in figure 1(*b*). This vortex also exhibits $n = 1$ spirals that, unlike for the OCV, reach to the surface (see figure 5*e* of F09). As a result of these asymmetries, the DVJ was observed to wander away from the centre axis. Similar wandering was observed in a laboratory vortex model by Zhang & Sarkar (2012). For the DVJ case, the temporal–azimuthal mean was computed relative to the centre of the displaced circulation.

For the slightly smaller value of $f = 0.15$ and the significantly smaller value of $\nu = 0.0001$, the simulations of F09 produce a 'high swirl' or 'two-celled vortex' (hereafter, TCV) with the mean flow shown in figure 1(*c*). Here, the central downdraft has penetrated very close to the surface and there is a very large overshoot of the radial inflow in the boundary layer followed by a large rebound out to a larger updraft radius. The designation of a vortex as 'two-celled' is usually meant to imply that the radial inflow layer fully separates at non-zero radius and there is downward recirculation all the way to the surface, and perhaps even low-level outflow at small radius. These numerical simulations and others with no-slip lower boundary conditions (e.g. Fiedler 1998; Nolan 2005*b*) produce transient flow structures with full separation but they are not sustained in the time mean. Simulations with a turbulent 'bulk drag law' or other 'semi-slip' lower boundary conditions such as those of Lewellen *et al.* (2000) appear to come closer to separation of the boundary layer and a fully two-celled structure, but in the time mean there still appears to be some radial inflow reaching the centre axis (see figure 1*e* of Lewellen *et al.* 2000). In any case, while low-reflectivity regions observed in tornadoes by portable Doppler radar are good indications of TCV structure above the surface (the so-called 'weak echo hole': Wurman, Straka & Rasmussen 1996; Bluestein & Pazmany 2000), whether or not radial inflow in the lowest 0–50 m consistently penetrates to the centre axis or separates from the surface in real tornadoes remains unknown.

More to the point, the dynamics of the vortex we designate here as the TCV are quite different from the OCV and DVJ. For the OCV, there is an axial jet extending from the surface to $z = 0.16$ with peak $W = 1.6$; for the DVJ, this extends to $z = 0.1$ with a peak $W = 0.32$; while for the TCV it extends only to $z = 0.035$ with peak $W = 0.05$. More importantly, the TCV does indeed break down into multiple vortices that attach to the surface, as shown in figure 4(*e*) of F09.

2.2. *Temporal mean of a symmetric simulation*

We also consider the temporal-mean state of a purely axisymmetric simulation using the domain and parameters of the DVJ. This simulation was performed using the axisymmetric incompressible flow model of NF99*b*, modified to allow for vertically varying viscosity. Rather than the stretched grids of Fiedler (2009), this model uses regular grid spacing with 256 points in each direction; the grid spacings are $\Delta r = 0.0078$ and $\Delta z = 0.0039$. These spacings are about twice as large as the minimum grid spacings of Fiedler (2009), but those smaller grid spacings are only

necessary to resolve the boundary layer of the TCV. The time-mean flow generated by this simulation, hereafter referred to as AXI-DVJ, is shown in figure 1(*d*). The low-level structure is very similar to that of DVJ, but peak wind speed is slightly less, the vortex is slightly larger, and the flow field is slightly more peaked (in both V and W) across the updraft axis. Inside the updraft region, the flow is much weaker. Above the vortex core, the 'outflow' turns outward toward larger radius at a much sharper angle for AXI-DVJ than for all of the other vortices.

3. Linear stability analysis

The numerical method for linearized stability analysis is nearly identical to that used in Nolan (2005*a*), so we will only summarize the procedure here. The incompressible equations of motion in cylindrical coordinates are linearized about basic-state flows $U(r, z)$, $V(r, z)$ and $W(r, z)$. (Variables with capital letters refer to the basic-state wind field about which the equations are linearized.) This produces equations for the perturbation velocity fields $u'(r, \lambda, z, t)$, $v'(r, \lambda, z, t)$, $w'(r, \lambda, z, t)$ and the perturbation pressure $p'(r, \lambda, z, t)$, where λ is the angle around the azimuth. Each of the four perturbation variables are then decomposed into their contributions from a Fourier series for each azimuthal wavenumber n, e.g.

$$u'(r, \lambda, z, t) = u_n(r, z, t)\mathrm{e}^{\mathrm{i}n\lambda}. \tag{3.1}$$

For each wavenumber n, including $n = 0$ (corresponding to axisymmetric perturbations), this generates three momentum equations for u_n, v_n and w_n, and an incompressibility condition; the momentum equations also contain the perturbation pressure field p_n. For $n \geqslant 1$, v_n and p_n can be eliminated using the incompressibility condition and the two equations that result are for u_n and w_n. For $n = 0$, v_n does not appear in the incompressibility equation, so it cannot be eliminated. Instead, the u_0 and w_0 equations are cross-differentiated and then combined to eliminate the symmetric perturbation pressure p_0. Using the symmetric incompressibility equation, the resulting equation can be expressed as an equation for the axisymmetric streamfunction ψ_0.

For this study, the equations of Nolan (2005*a*) were modified to incorporate the effect of the background rotation rate via the Coriolis parameter $f = 2\Omega$, where here Ω is the non-dimensional background rotation rate that varies among the F09 numerical simulations. This turns the angular velocity term $2\Omega = 2V/r$ in the Nolan (2005*a*) equations into $2V/r + f$. The diffusion terms were extended to allow for spatially varying ν in the diffusion operators, to match the vertically varying ν of F09.

The linearized equations are solved on an Arakawa-C-type staggered grid that covers the (r, z) domain defined by $0 \leqslant r \leqslant 2$ and $0 \leqslant z \leqslant 1$. For computational efficiency (and necessity), the grid-stretching algorithm described in Appendix B of Nolan & Montgomery (2002*b*) is used. This algorithm generates a smoothly varying grid spacing that follows the shape of the hyperbolic tangent function between the regions of small and large grid spacing. The grids are defined by the ratios (α_r and α_z) of the smallest to largest grid spacing, and the location of transition region between them (σ_r and σ_z). The staggered, stretched grids and their parameter values are shown in figure 2. The same grid is used for the OCV and the DVJ, while for the TCV the parameters were adjusted to bring even more grid points closer to the surface. The grids used for the actual computations have 81×81 points, four times as many points in each direction as the grids shown in figure 2. The smallest radial grid spacing for all cases is $\Delta r = 0.01$; for the OCV and DVJ, the smallest $\Delta z = 0.005$, while for the TCV the smallest $\Delta z = 0.0027$.

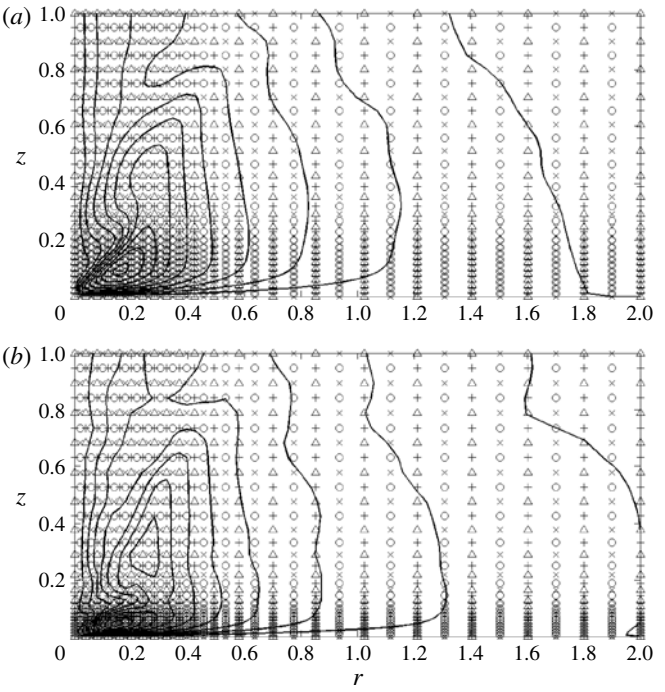

FIGURE 2. The domain and stretched grid configurations for the analyses of the unstable modes, for (*a*) OCV and DVJ with stretching parameters $\alpha_r = 0.2$, $\sigma_r = 0.5$, $\alpha_z = 0.5$ and $\sigma_z = 0.25$; and (*b*) for the TCV with $\alpha_r = 0.2$, $\sigma_r = 0.5$, $\alpha_z = 0.1$, $\sigma_z = 0.25$. Contours of the mean azimuthal flow are also shown for the DVJ and TCV cases. (+) marks the locations of u velocities, (×) marks the locations of w, (○) marks the locations of v and p, and (△) marks the locations of h and y. These figures have 41 points in the radial and vertical directions on the 'master grid', which contains all four subgrids, each of which have half the points of the master grid. The actual grids used for calculations in this paper had four times as many points in both directions.

Rather than growing unstable modes from time evolution of the linearized equations, these stability analyses are performed by constructing a matrix operator representation of a finite-difference approximation to the linearized dynamics. Unstable modes are selected from the complete set of eigenvalues and eigenvectors of the time evolution operator as computed by standard methods. (Matlab 7.11 was used for all calculations.) While computationally demanding, this has the advantage that it identifies *all* the modes of a particular configuration, e.g. the 'second most unstable' and 'third most unstable' modes can be examined.

The boundary conditions used in the linearized stability calculations are as in F09: the lower boundary condition is impermeable for w_n and no-slip for u_n, v_n, while the upper and outer boundaries are impermeable for normal velocities and free-slip for parallel velocities. The implementation of free-slip, no-slip, and $r = 0$ boundary conditions is discussed in Appendix B of Nolan & Grasso (2003) and § 3.2 of Nolan (2005*a*).

4. Results

Figure 3 shows the growth rates of the most unstable modes (MUMs) for $n = 0$ to $n = 8$ for each of the four vortices. First, we consider the stability properties and

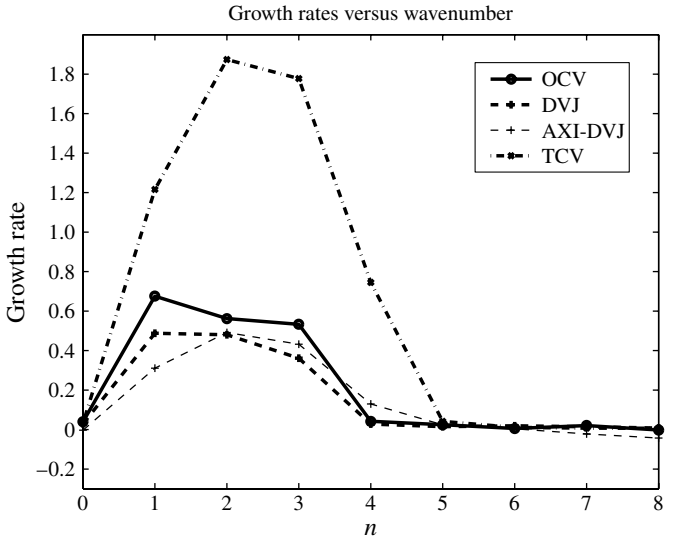

FIGURE 3. The growth rates of the most unstable modes (MUMs) for each azimuthal wavenumber, in units of non-dimensional inverse time, for the one-celled vortex (OCV), the drowned vortex jump (DVJ), the two-celled vortex (TCV), and an axisymmetric simulation of the drowned vortex jump (AXI-DVJ).

MUMs for the three mean states from the three-dimensional model. The AXI-DVJ case will be discussed in the final subsection.

4.1. *The one-celled vortex (OCV)*

For the OCV, there is a weak instability for $n = 0$, and then much greater growth rates for $n = 1$, 2 and 3. The growth rates are in units of inverse non-dimensional time, and the inverses of the growth rates are *e*-folding times. For $n = 1$, 2 and 3, these *e*-folding times are 1.48, 1.78 and 1.88, respectively. Given that the peak non-dimensional wind speed of the OCV is ∼1.0 at a radius of maximum azimuthal winds (hereafter, RMW) of 0.05 (see figure 1*a*), the vortex circulation time scale $\tau_{circ} = (2\pi \times 0.05)/1.0 = 0.318$. Thus, the *e*-folding times of these modes correspond to ∼5 circulation times in the vortex core.

To visualize the structure of the MUM, figure 4(*a,b*) depicts radius–height plots of the real and the imaginary parts of the perturbation velocities for $n = 1$, shown as contours of v_n and vectors $[u_n, w_n]$ of the meridional circulation. The stability analysis assumes the following harmonic form:

$$v_n(r, \lambda, z, t) = v_n(r, z) \exp\{st + in\lambda\} = v_n(r, z) \exp\{s_r t\} \exp\{in\lambda + is_i t\} \qquad (4.1)$$

where s_r and s_i are the real and imaginary parts of the eigenvalue s. All the asymmetric modes shown here and below have negative s_i and thus turn in the counterclockwise (cyclonic) direction with the basic-state flow. (This is opposite to the usual convention which uses $\exp\{in\lambda + i\omega t\}$ and counterclockwise turning is indicated by a positive real part of ω.) At each angle λ the physical solution is presumed to be the real part of (4.1); for $\lambda = 0$ (i.e. along the x-axis in the positive direction) this is equal to

$$v_n(r, \lambda, z, t) = \exp(s_r t)[\mathrm{Re}\{v_n\} \cos(s_i t) - \mathrm{Im}\{v_n\} \sin(s_i t)]. \qquad (4.2)$$

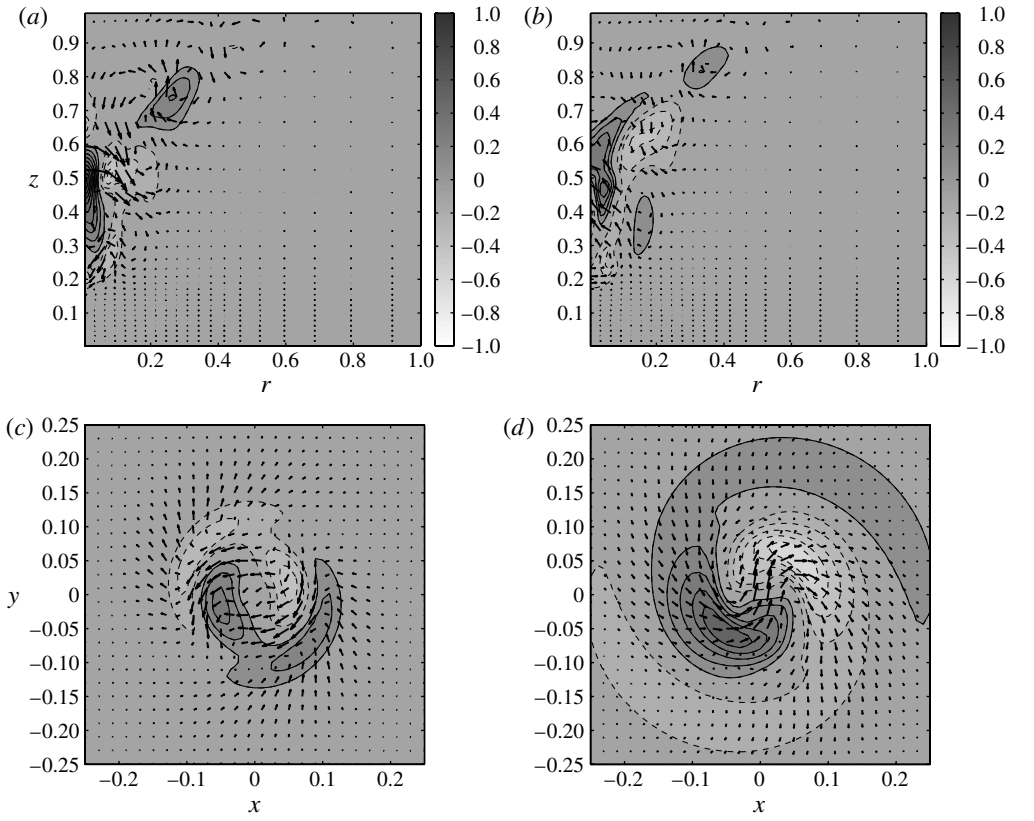

FIGURE 4. Structure of the MUM for $n = 1$ in the OCV: (*a*) r–z cross-section of the real part, with contours of azimuthal velocity and wind vectors of radial and vertical velocity; (*b*) r–z cross-section of the imaginary part; (*c*) horizontal cross-section at $z = 0.25$, with contours of w_1 and vectors of horizontal flow; (*d*) horizontal cross-section at $z = 0.5$. Extreme values of the contoured fields, the amplitude of the largest vector, and the contour interval are: (*a*) max $= 1$, min $= -0.43$, int $= 0.1$, maxvec $= 0.56$; (*b*) max $= 0.49$, min $= -0.32$, int $= 0.1$, maxvec $= 1$; (*c*) max $= 0.35$, min $= -0.35$, int $= 0.10$, maxvec $= 0.33$; (*d*) max $= 0.59$, min $= -0.59$, int $= 0.10$, maxvec $= 0.94$.

Thus for negative s_i, $v_n(r, \lambda, z, t)$ along $\lambda = 0$ evolves in time from $\mathrm{Re}\{v_n\} \rightarrow \mathrm{Im}\{v_n\} \rightarrow -\mathrm{Re}\{v_n\} \rightarrow -\mathrm{Im}\{v_n\}$. In other words, the imaginary part corresponds to the structure that is 90° in phase 'upstream' of the real part (or, 90° into the 'future'), so as the mode rotates cyclonically, it is the phase that will appear next. Each mode has been normalized so that the maximum of the absolute value of v_n is 1, and is rotated so that this value occurs for azimuth angle $\lambda = 0$.

For $n = 1$ it is apparent that the MUM exists entirely *above* the low-level vortex core. Although the time- and azimuthal-mean flow is unstable in the global sense, these instabilities do not grow near the surface, such that the low-level flow remains essentially laminar. Fiedler & Rotunno (1986) and Fiedler (1989) have argued that it is the strong vertical advection by the axial jet coming up out of the low-level vortex that prevents downstream influence. An additional stabilizing factor may be the strong radial inflow itself. Nolan & Farrell (1999*a*) and Nolan (2001) found that radial inflow damps the growth of asymmetric modes on an unstable vortex.

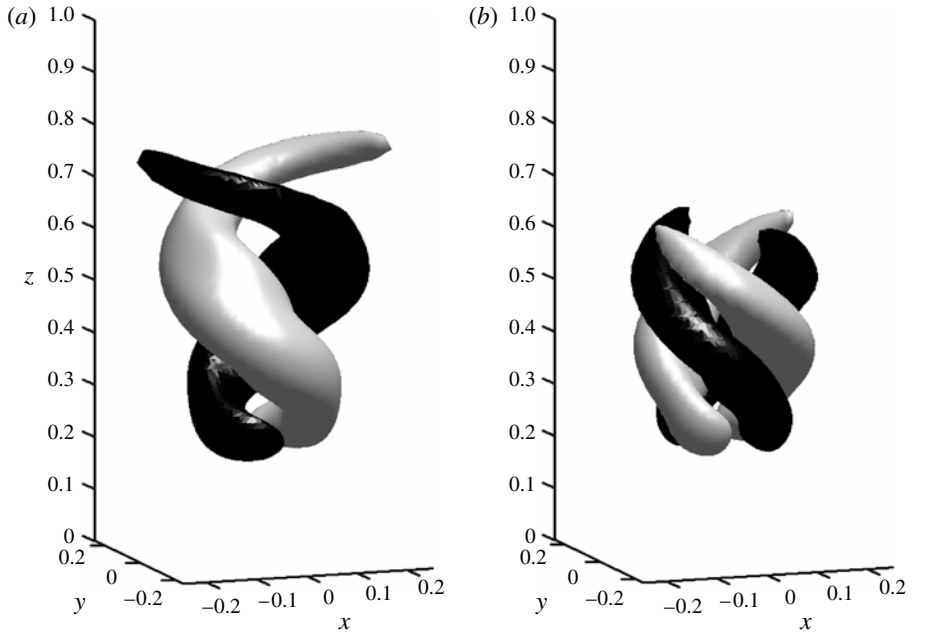

FIGURE 5. Three-dimensional renderings of surfaces of constant perturbation pressure ± 0.075 for the MUMs in the OCV: (*a*) $n = 1$; (*b*) $n = 2$.

Figure 4(*a*) also shows that the $n = 1$ mode has large perturbation values at the $r = 0$ axis. This is a special property of $n = 1$ asymmetries, in that they can (and usually do) exhibit flow across the centre axis, while for all other modes ($n = 0$ and $n > 1$) perturbation velocities go to zero at the centre axis. For this reason, $n = 1$ modes are almost always associated with some degree of displacement of the vortex centre from its original axis.

The flow across the centre axis is better illustrated by horizontal cross-sections, as seen in figure 4(*c*,*d*), which shows contours of w_n and horizontal flow vectors $[v_x, v_y]$, where v_x and v_y are the flow speeds in Cartesian coordinates. The cross-sections are shown at $z = 0.25$ and $z = 0.5$. At the lower level, the asymmetric structure of the mode is typical for a quasi-two-dimensional barotropic instability, with two asymmetric waves at different radii, phase shifted so that each wave is favourably configured to amplify the other wave (Staley & Gall 1979; Schubert *et al.* 1999; Nolan & Montgomery 2002*b*; Terwey & Montgomery 2002). At the upper level, the mode exhibits a very different structure. While there is strong flow across the axis, the vertical velocities consist of a single wave that spirals outward.

Returning to figure 4(*a*), it can be seen that there are three overturning circulations in $[u_n, w_n]$ extending upward and outward along the outflow of the basic-state vortex. In fact, these overturnings along the upper-level outflow are produced by a single spiral vortex that turns clockwise with height. The structure of the mode can be seen better with a three-dimensional visualization of a surface of constant perturbation pressure. Swirling motion around an axis of strong vorticity generates negative or positive dynamic pressures, depending whether the sign of the vorticity perturbation is the same or opposite to the basic-state flow, respectively (see § 8.4.5 of Markowski & Richardson 2010). For the MUM for $n = 1$, figure 5(*a*) shows surfaces of perturbation

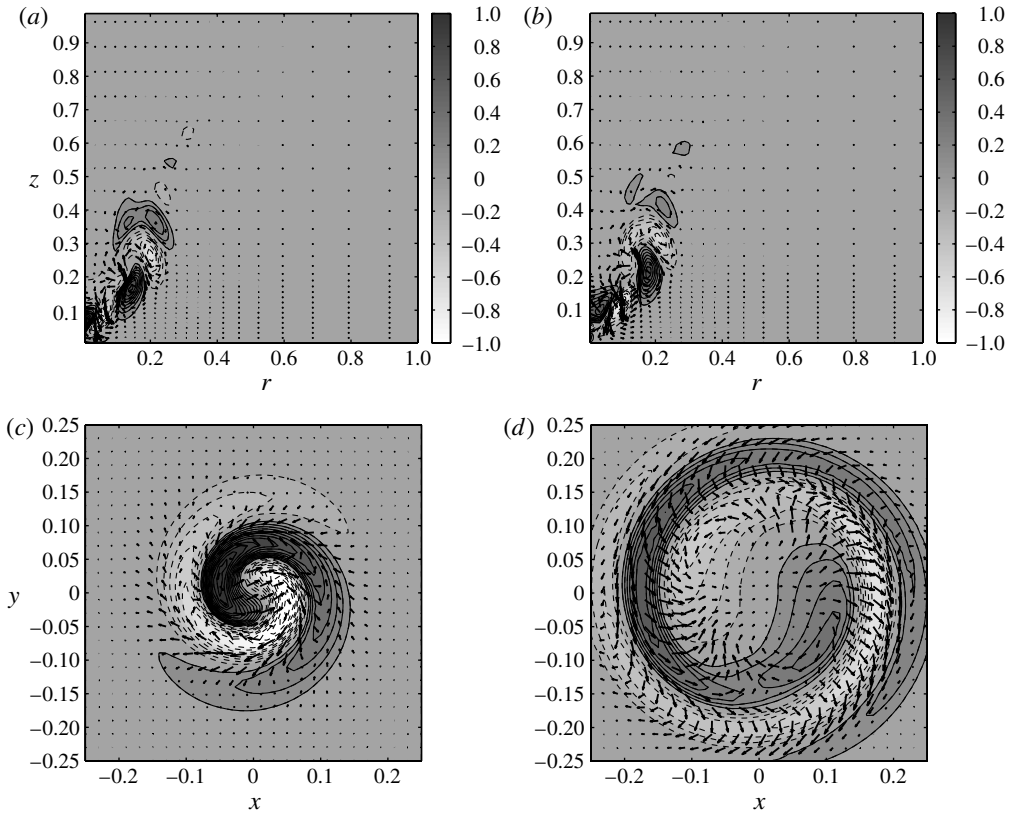

FIGURE 6. Structure of the MUM for $n = 1$ in the DVJ vortex: (*a*) r–z cross-section of the real part, with contours of azimuthal velocity and wind vectors of radial and vertical velocity; (*b*) r–z cross-section of the imaginary part; (*c*) horizontal cross-section at $z = 0.10$, with contours of w_1 and vectors of horizontal flow; (*d*) horizontal cross-section at $z = 0.27$. (*a*) max = 1, min = −0.76, int = 0.1, maxvec = 1.4; (*b*) max = 0.75, min = −0.83, int = 0.1, maxvec = 1.1; (*c*) max = 1.30, min = −1.30, int = 0.10, maxvec = 0.85; (*d*) max = 0.68, min = −0.68, int = 0.10, maxvec = 0.64.

pressure equal to 0.075 and −0.075 non-dimensional units. The spiral structure of the mode and its clockwise turning with height can be seen. The corresponding plot for the MUM for $n = 2$ is shown in figure 5(*b*). This mode is more compact and it does not extend as far upward as the $n = 1$ mode, but like the $n = 1$ mode it has no signature below $z = 0.2$.

As seen in figure 3, the stability analysis also finds that there is an unstable symmetric mode. The symmetric modes for each of the three vortices will be discussed together in § 4.5.

4.2. *The drowned vortex jump (DVJ)*

As shown in figure 3, the MUM occurs for $n = 1$ in the DVJ, but it is nearly matched in growth rate by the most unstable node for $n = 2$. The e-folding times of the $n = 1$ and $n = 2$ MUMs are 2.06 and 2.08, respectively; $\tau_{circ} = 1.06$ for this vortex. The real and imaginary parts of the $n = 1$ mode, normalized and rotated as above, are shown in figure 6. Also shown are horizontal cross-sections of the mode at $z = 0.1$ and $z = 0.27$.

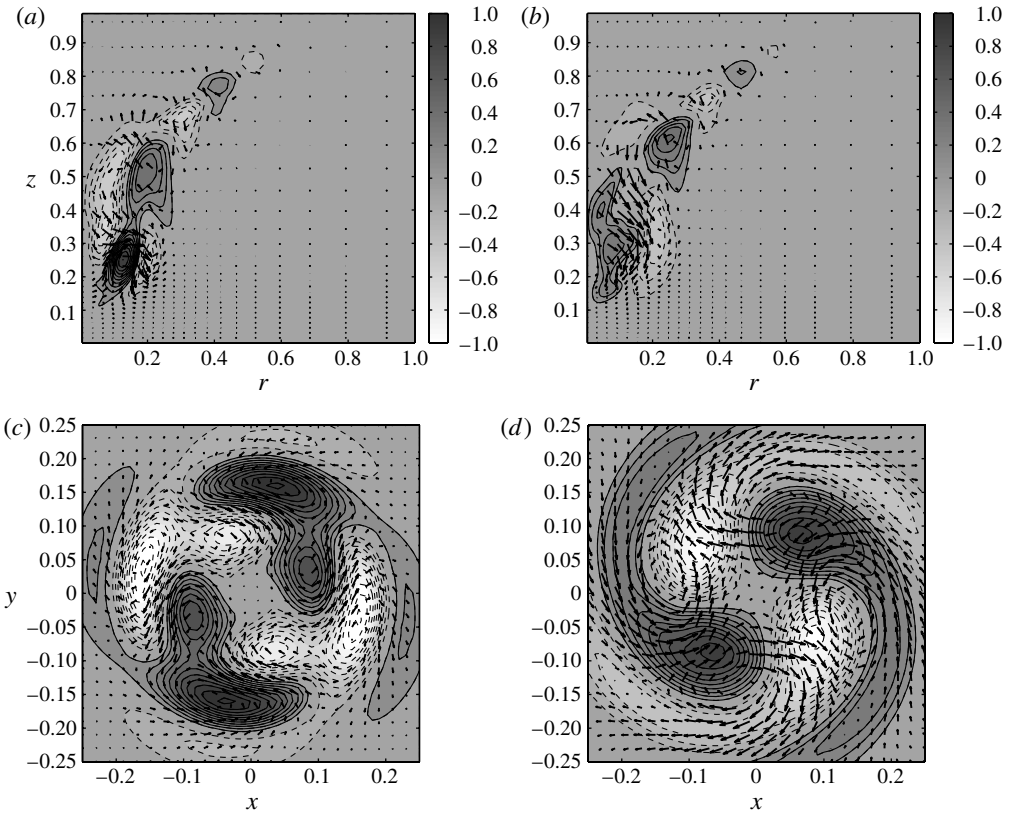

FIGURE 7. Structure of the MUM for $n = 2$ in the DVJ vortex: (*a*) r–z cross-section of the real part, with contours of azimuthal velocity and wind vectors of radial and vertical velocity; (*b*) r–z cross-section of the imaginary part; (*c*) horizontal cross-section at $z = 0.25$, with contours of w_2 and vectors of horizontal flow; (*d*) horizontal cross-section at $z = 0.50$. (*a*) max $= 1$, min $= -0.53$, int $= 0.1$, maxvec $= 1.1$; (*b*) max $= 0.53$, min $= -0.40$, int $= 0.1$, maxvec $= 1$; (*c*) max $= 1.14$, min $= -1.14$, int $= 0.10$, maxvec $= 1.14$; (*d*) max $= 0.95$, min $= -0.95$, int $= 0.10$, maxvec $= 0.57$.

At the lower level, the mode has strong flow across the centre axis, indicating that the mode would excite a growing displacement of the vortex core. The mode has a spiral structure with upward and outward spiral arms of meridional overturning both at the lower and upper levels.

As shown in figure 7, the $n = 2$ mode is quite different. The mode exists well above the low-level vortex core, indicating that $n = 2$ asymmetries would only appear above the boundary layer. At $z = 0.25$, the mode has the structure of a two-dimensional instability with two phase-shifted asymmetric waves at different radii. At $z = 0.5$ and above the mode transitions to spiral overturnings.

These differences in the $n = 1$ and $n = 2$ modes for the DVJ vortex are further illustrated in three-dimensional isosurfaces of perturbation pressure (figure 8). In each case, the value of perturbation pressure used for the surfaces has been chosen subjectively to best illustrate the structures. For $n = 1$, a 'low and tight' spiral structure is revealed. For $n = 2$, the mode has the more two-dimensional, barotropic structure at low levels (although still tilting back against the shear). Above $z = 0.35$, it transitions to spiral overturnings, as indicated in figure 7(*d*).

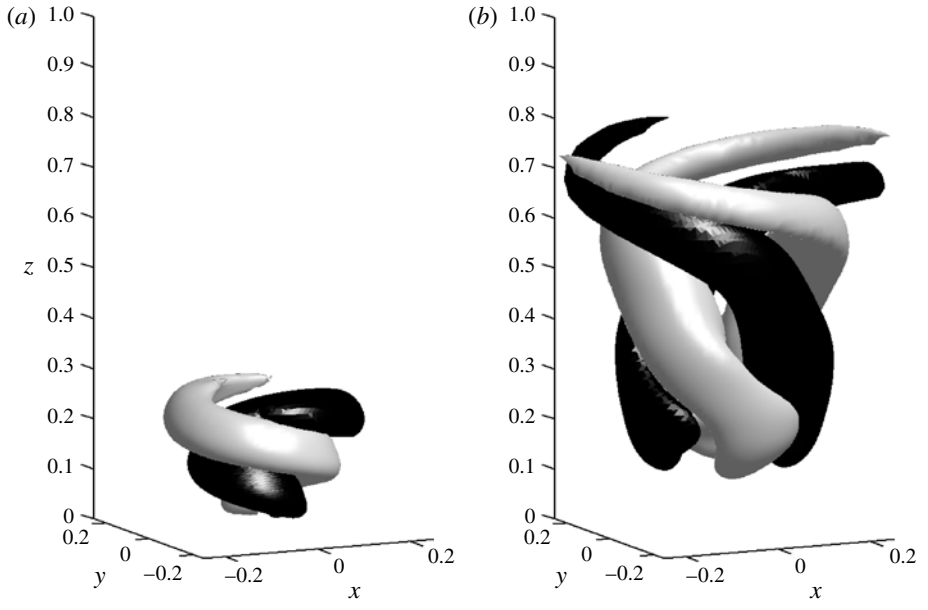

FIGURE 8. Three-dimensional renderings of surfaces of constant perturbation pressure for the MUMs in the DVJ vortex: (*a*) $n = 1$, ± 0.125 isosurfaces; (*b*) $n = 2$, ± 0.075 isosurfaces.

4.3. *The two-celled vortex (TCV)*

The MUMs for the TCV consist entirely of 'low and tight' spirals that exist just above the low-level wind speed maximum at $r = 0.14$, $z = 0.04$ (see figure 1*c*). The vertical and horizontal structures of the $n = 2$ and $n = 3$ MUMs are shown in figure 9. The peak vertical velocities (1.32, and 1.59, respectively) are significantly larger than the peak azimuthal velocities (normalized to 1 for both modes), indicating that the spiral overturning motions dominate the two-dimensional asymmetric motions. It is noteworthy that the locations of these modes match closely with the region of maximum velocity variance in the TCV simulations of Lewellen *et al.* (2000, see their figure 1*a*), even though those simulations had a pronounced $n = 7$ asymmetry.

These structures are also shown as isosurfaces of perturbation pressure in figure 10. For $n = 3$, the low-level spiral appears to be attached to more upright structures that emanate upward at a smaller angle from the vertical. These correspond to the upward extension of v_n as seen near $r = 0.175$, $z = 0.25$ in figure 9(*a*).

Looking at the structure of the basic-state wind field for the TCV (figure 1*c*), there are two distinct maxima of V. The first is associated with the low-level jet, with strong radial inflow and outflow immediately below and above it, respectively. The second is the elevated wind maximum around $r = 0.25$, $z = 0.3$, with a strong updraft on its radially inward side. Such dual maxima of the azimuthal wind field were recently inferred in observational analyses by Wakimoto, Atkins & Wurman (2011). The upward extension of the $n = 3$ MUM suggests that it is trying to exploit the potential for energy extraction from this flow region. As it turns out, the 'second MUM' for $n = 3$ primarily taps into the instability of this region. This mode, which has a growth rate of 0.31 ($\sim$1/6th of the MUM), is shown in figure 11. The existence of this mode suggests that the TCV is susceptible to two distinct sets of instabilities. The first and most unstable set of modes are the 'low and tight' spirals that live on

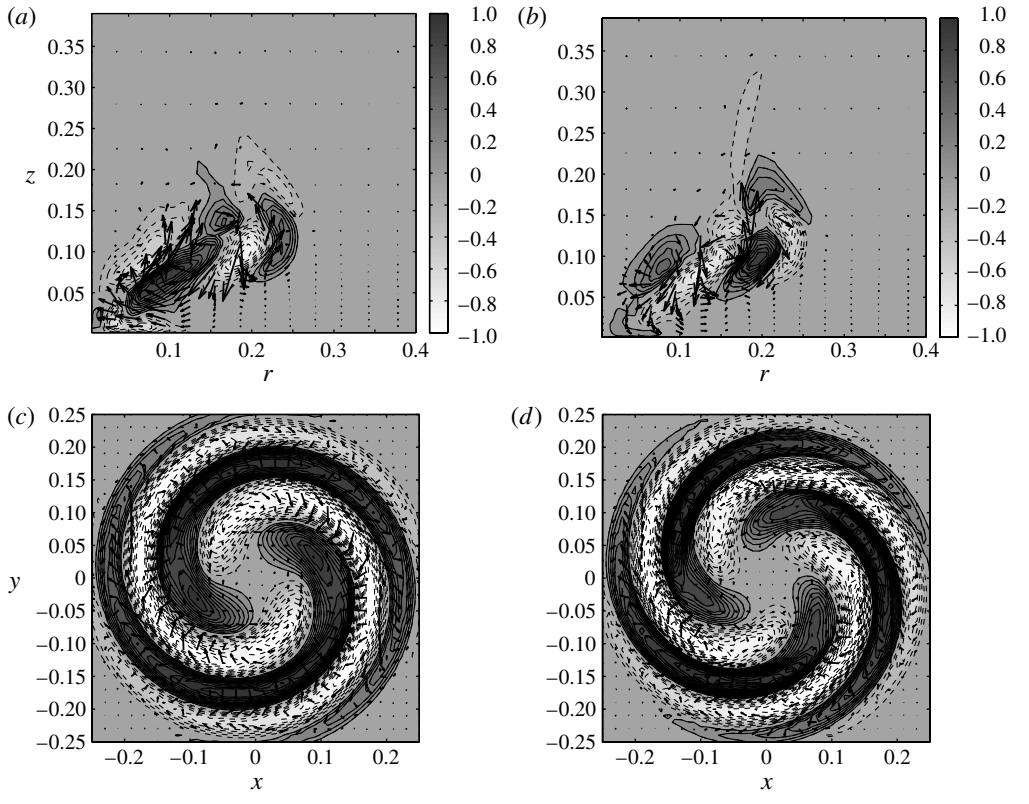

FIGURE 9. Structures of the $n = 2$ and $n = 3$ MUMs in the two-celled vortex: (*a*) r–z cross-section of the real parts of u and $[v, w]$ for $n = 2$ and (*b*) for $n = 3$; (*c*) horizontal cross-section of w and $[u, v]$ at $z = 0.10$ for $n = 2$ and (*d*) for $n = 3$. (*a*) max $= 1$, min $= -0.86$, int $= 0.1$, maxvec $= 1.7$; (*b*) max $= 1$, min $= -0.79$, int $= 0.1$, maxvec $= 1.7$; (*c*) max $= 1.32$, min $= -1.32$, int $= 0.10$, maxvec $= 1.05$; (*d*) max $= 1.59$, min $= -1.59$, int $= 0.10$, maxvec $= 1.13$.

the low-level wind maximum, as exemplified by figure 10(*a*). A second set of less unstable modes may appear further above in the secondary, elevated wind maximum and its associated axial jet. Like some of the modes shown previously, these modes are a mix of quasi-two-dimensional and spiral structures.

4.4. *Symmetric modes*

We first examine the $n = 0$ MUM for the OCV. The eigenvalues and eigenvectors for this mode also have both real and imaginary parts. When the eigenvalues and eigenvectors for $n = 0$ have imaginary parts, they are always paired with a conjugate eigenvalue and eigenvector. When the two conjugate modes are summed together, the imaginary parts of the two solutions exactly cancel, ensuring that the perturbations are entirely real, with the same time evolution as (4.2). If we choose the symmetric mode with $s_i < 0$, the time evolution of the symmetric perturbations will also evolve as $\mathrm{Re}\{v_n\} \to \mathrm{Im}\{v_n\} \to -\mathrm{Re}\{v_n\} \to -\mathrm{Im}\{v_n\}$.

Figure 12 shows the real and imaginary parts of the $n = 0$ MUM with $s_i < 0$. The real part shows a symmetric overturning with radial inflow near the centre axis between $z = 0.1$ and $z = 0.2$, with compensating radial outflow above. Accompanying

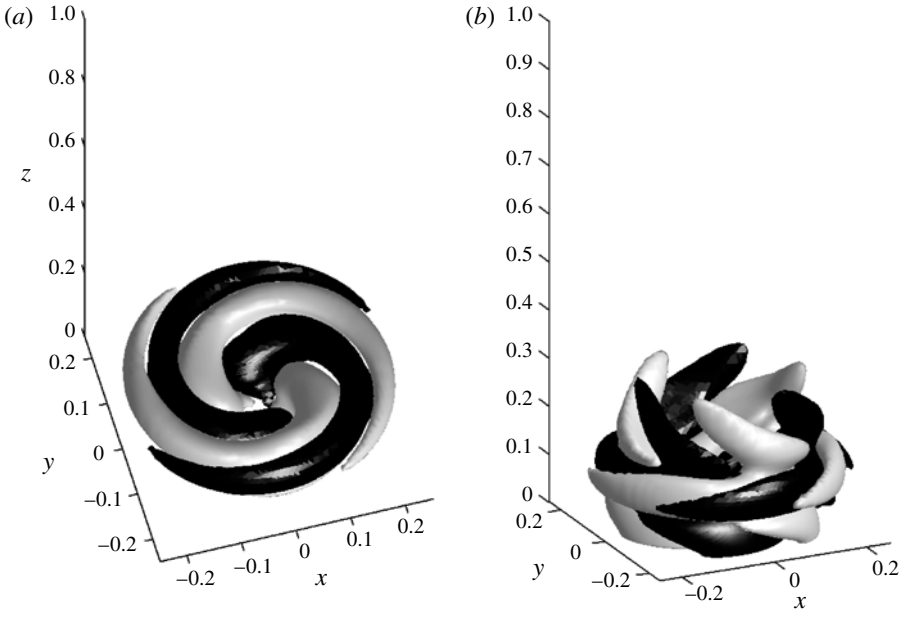

FIGURE 10. Three-dimensional renderings of surfaces of constant perturbation pressure for MUMs in the two-celled vortex: (*a*) for $n = 2$, perturbation pressure $= \pm 0.05$; (*b*) for $n = 3$, perturbation pressure $= \pm 0.02$, at a different viewing angle.

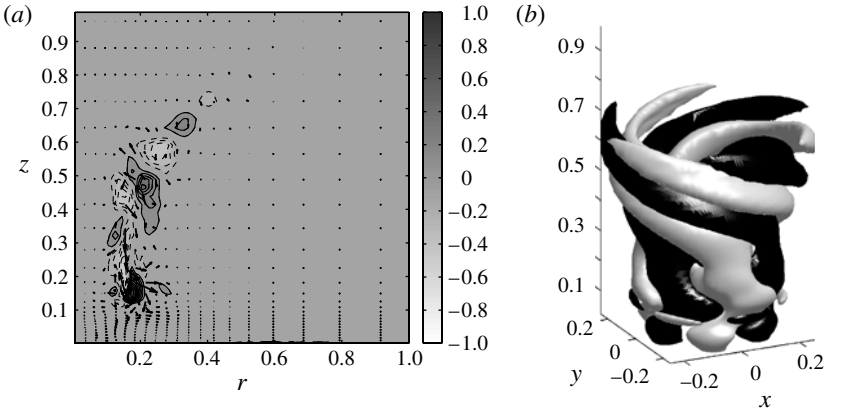

FIGURE 11. Vertical structure of the second-MUM for $n = 3$ in the two-celled vortex: (*a*) r–z cross-section of the real parts of v_3 and $[u_3, w_3]$ (max $= 1$, min $= -0.53$, int $= 0.1$, maxvec $= 0.77$); (*b*) isosurfaces of constant perturbation pressure $= \pm 0.0015$.

the radial inflow and outflow is a couplet of intensification and weakening of the azimuthal wind below and above $z = 0.2$, respectively. Comparing this structure to the basic-state flow (figure 1*a*), it appears that this phase of the mode corresponds to an intensification and upward expansion of the peak azimuthal wind in the vortex core, while at the same time the circulation immediately above is weakened. Interestingly, the meridional flow vectors of the mode extend the full length of the outflow, suggesting that this phase of the oscillation corresponds to an intensification of the

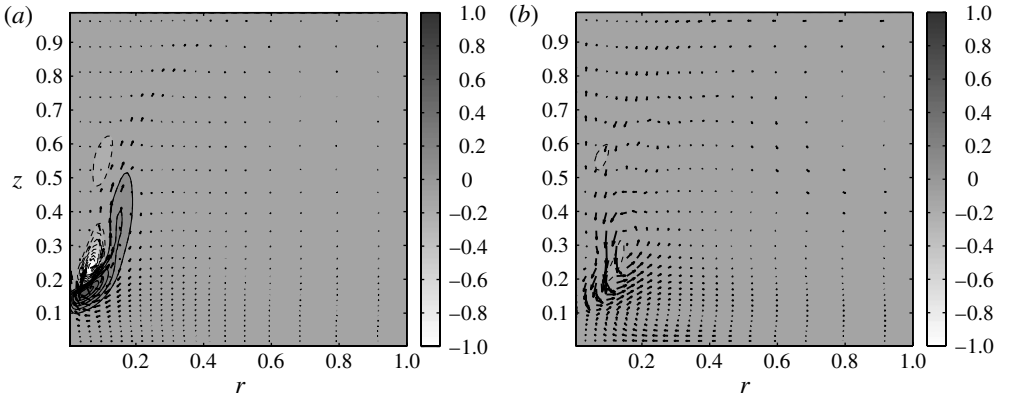

FIGURE 12. Real (a) and imaginary (b) parts of the MUM for symmetric ($n = 0$) motions in the OCV, v_0 and $[u_0, w_0]$. (a) max $= 0.68$, min $= -1$, int $= 0.1$, maxvec $= 0.85$; (b) max $= 0.068$, min $= -0.12$, int $= 0.1$, maxvec $= 0.23$.

entire inner-core circulation. After showing this phase, the mode would then evolve to the imaginary part shown in figure 12(b). This phase contains an overturning that is in the reverse direction to the previous phase, but also shifted slightly upward. There is virtually no perturbation v_0, with the previous anomalies apparently having been cancelled out due to advection by the reversing circulation. The next phase would be the opposite of the real part shown in figure 12(a), which would indicate a lowering of the inner-core vortex and a weakening of the overall circulation, followed by a transition to the amplifying phase and a positive circulation leading again to amplification of the inner-core vortex.

The growth rate is much slower than for the asymmetric modes, with an e-folding time of 25.5 or $\sim 80\tau_{circ}$, so it would probably equilibrate at a fairly low amplitude and it would not play a significant role in the nonlinear evolution of the vortex. However, its peak amplitude occurs around $z = 0.15$, which is well below the peak amplitude of the $n = 1$ and $n = 2$ modes. We would expect this mode to reveal itself as a symmetric oscillation of the depth and intensity of the low-level, inner-core vortex below the asymmetric spiral modes shown in figure 5. The frequency of this oscillation would be $2\pi/s_i = 11.8$ non-dimensional time units, corresponding to $\sim 37\tau_{circ}$.

Symmetric oscillations of tornado wind fields have in fact been observed. Bluestein *et al.* (2003) show the time evolution of the azimuthal-mean winds of a tornado observed by portable Doppler radar. The peak winds were observed to increase and decrease on a time period of 1 to 2 min, and these variations were correlated with decreases and increases (respectively) of the RMW. Using their observed peak azimuthal-mean wind speeds of 25 m s^{-1} and RMW of 200 m the fastest τ_{circ} in that tornado was approximately 50 s. Therefore, the oscillations occur on the order of 1–$2\tau_{circ}$, which is clearly much faster than the oscillation frequencies computed above.

Tanamachi *et al.* (2007) also observed oscillations in the size of the low-reflectivity core of a tornado that can be taken as an indicator of changes in the size of the inner core. The periods of these oscillations ranged between 1 and 2 min. The peak azimuthal-mean wind also showed oscillations with a time scale of 1 to 2 min, and at some times (but not all) the wind maxima were correlated with size minima. This tornado was smaller (RMW $\sim$ 60 m) and stronger ($V \sim 40$ m s^{-1}) so its τ_{circ} was approximately only 9 s. In this case the period of the oscillations corresponds to

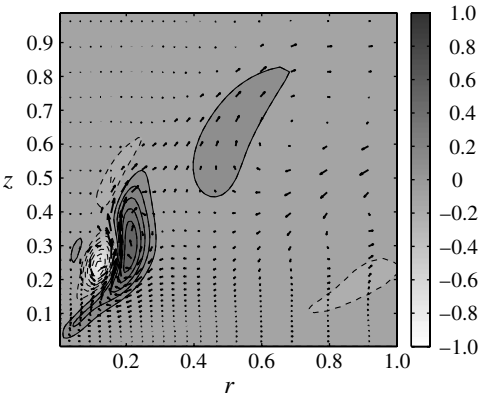

FIGURE 13. The MUM for symmetric ($n = 0$) motions v_0, $[u_0, w_0]$ in the DVJ vortex. max = 0.6, min = −1, int = 0.1, maxvec = 1.

7–14τ_{circ}, still rather far from the oscillation time scale for the $n = 0$ MUM described above.

However, the OCV supports additional $n = 0$ modes that oscillate with higher frequencies. The third most unstable mode has an e-folding time that corresponds to 102τ_{circ} and an oscillation period of 26τ_{circ}; the fourth most unstable mode has an e-folding time of 320τ_{circ} and an oscillation period of 21τ_{circ}. The structures of these modes are nearly identical to the MUM shown in figure 12. All of the symmetric modes, including the MUM, grow very slowly and thus are effectively neutral modes. In this case the mode that dominates may instead be the mode with a frequency that matches best to external forcings. Also, the faster modes would be more easily observed since their time scales would be distinct from the evolution of the tornado vortex itself which can change on times scales of a few minutes or less.

Figure 13 shows the structure of the $n = 0$ MUM for the DVJ. The e-folding time of this mode is 34.2 and $\tau_{circ} = 1.06$ for the DVJ, so again the growth rate is fairly slow. Unlike for the OCV, both the eigenvalue and the eigenvector have only real parts. Thus, the interpretation of the $n = 0$ MUM for the OCV, where the real and imaginary parts represent phases of an undulation, does not apply. Rather, the result suggests that the basic-state flow of the DVJ vortex (figure 1*b*) would develop a growing symmetric overturning combined with the couplet of decreasing and increasing azimuthal velocities that are shown in figure 13.

How can we physically interpret this mode? It tells us that the basic state, which is a time and azimuthal mean of an unsteady simulation, would not be a stable solution for an equivalent purely axisymmetric numerical simulation. Rather, it would evolve toward something that is the sum of the basic state plus the flow structure of the mode (multiplied by some unknown amplitude). The difference between the desired steady state of the purely symmetric dynamics and the actual basic state is due to the accumulated effects of the linear and nonlinear waves and eddies. This will be shown explicitly in a later section.

The TCV supports unstable modes of both the stationary and oscillating types. The MUM for $n = 0$ has eigenvalue $s = 0.0316$, corresponding to an e-folding time of ∼34τ_{circ} (where $\tau_{circ} = 0.90$ for the TCV). The structure of this mode (figure 14*a*) suggests that purely axisymmetric dynamics would favour a wider and more intense circulation in the low-level jet, and a smaller and more intense circulation aloft. The

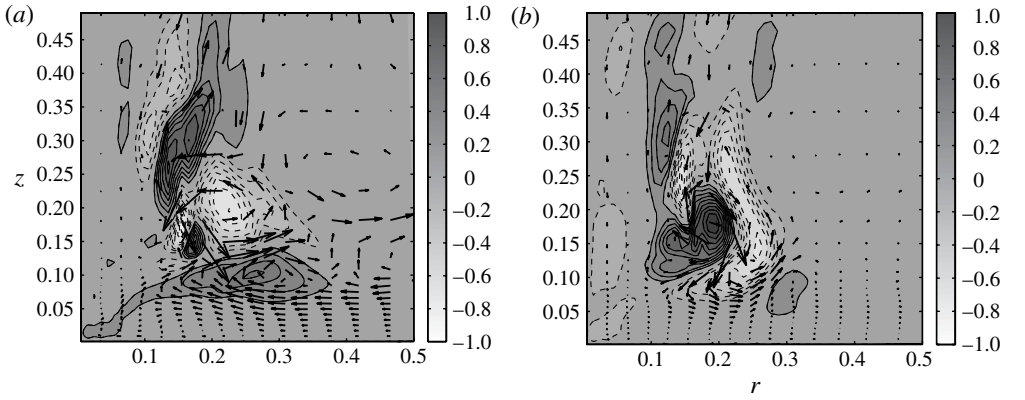

FIGURE 14. Real parts of the structures of the first (*a*) and eighth (*b*) MUMs for the $n = 0$ in the TCV, for v_0 and $[u_0, w_0]$. (*a*) max = 0.75, min = −1, int = 0.1, maxvec = 1; (*b*) max = 1, min = −0.71, int = 0.1, maxvec = 3.2.

second MUM (not shown) is a complex pair with an *e*-folding time of $56\tau_{circ}$ and an oscillation period of $53\tau_{circ}$. As for the OCV, weaker $n = 0$ instabilities exist with much faster time scales. The eighth MUM has an *e*-folding time of $\sim 1900\tau_{circ}$ (i.e. nearly zero growth rate), but an oscillation frequency of $20\tau_{circ}$. The real part of this mode is shown in figure 14(*b*), indicating that the oscillation would take the form of a contraction and expansion of the wind field above the boundary layer, with corresponding variations in the intensity of the secondary circulation. This mode does have some similarity with the oscillation observed by Tanamachi *et al.* (2007).

4.5. *Comparing to the simulations*

As noted above, the nonlinear simulations of F09 exhibit behaviours that are consistent with the results of our stability analyses: (i) the OCV and DVJ primarily show $n = 1$ asymmetric motions; (ii) the OCV is primarily laminar and axisymmetric at the surface, whereas the $n = 1$ asymmetries reach the surface in the DVJ vortex; and (iii) the TCV breaks down into two smaller vortices that spiral at large angles relative to the axis.

It is natural to wonder whether asymmetric structures similar to the unstable modes presented above actually appear in the simulations. For this purpose, the azimuthal-mean fields of figure 1 were interpolated back to Cartesian grids and then subtracted from three-dimensional model output to generate perturbation wind and pressure fields. As above, we find that perturbation pressure is the best field for viewing the structures of the asymmetries. Figure 15 shows such fields from arbitrarily selected times from the OCV, DVJ and TCV simulations. In each case, the viewing angle has been set to be the same as in the corresponding previous illustrations of the MUMs. Two plots are shown for the TCV, each having been chosen for their similarities with the renderings in figure 10(*a,b*), which emphasize the low-level and the mid-level structures, respectively. While the output from the nonlinear simulations is noisy and turbulent, there are clearly similarities with the linear modes.

4.6. *The axisymmetric drowned vortex jump (AXI-DVJ)*

While the stability curve for AXI-DVJ (see figure 3) is similar to that of DVJ, there are some significant differences in its stability and its modes. The MUM for $n = 1$ is

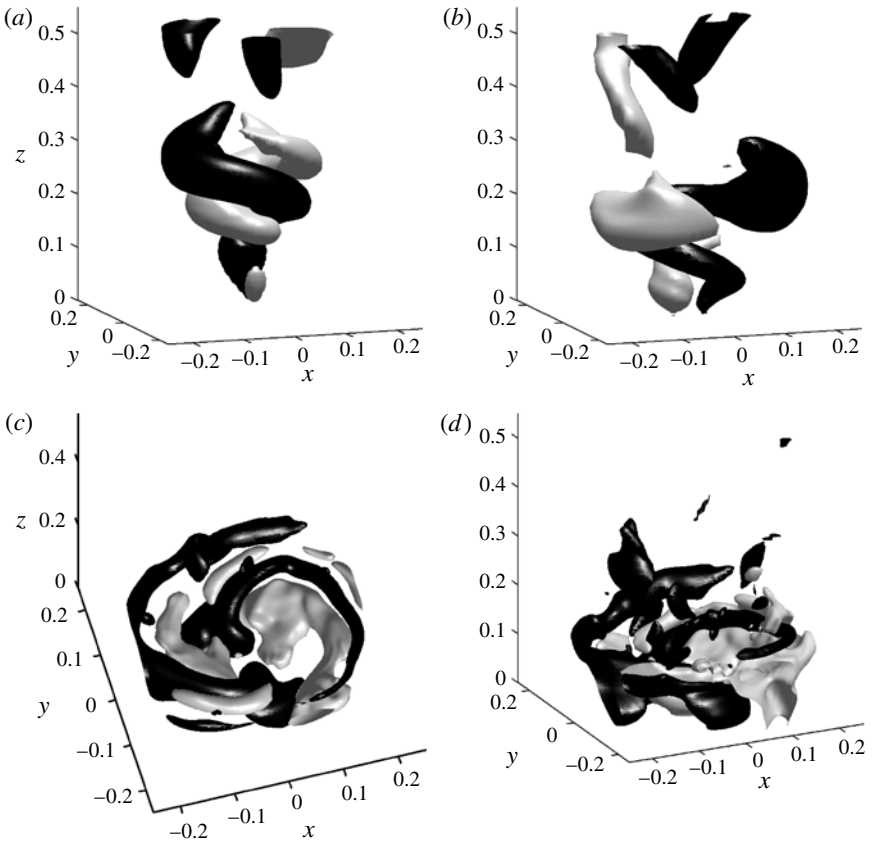

FIGURE 15. Isosurfaces of perturbation pressure from the nonlinear simulations of Fiedler (2009): (*a*) from the OCV simulation; (*b*) from the DVJ simulation; (*c*) from the TCV simulation; (*d*) from the TCV simulation, for a smaller pressure value and from a different viewing angle. Data for these images were only available from $z = 0$ to $z = 0.5$. (*a–c*) Perturbation pressure $= \pm 0.08$, (*d*) perturbation pressure $= \pm 0.05$.

less unstable so that $n = 2$ has the fastest growing MUM, and $n = 3$ and $n = 4$ are slightly more unstable. Figure 16 shows the real parts of the $n = 1$ and $n = 2$ MUMs. Although slightly elevated and at larger radius, the $n = 2$ MUM is similar in both vertical and horizontal (not shown) structure to its counterpart for DVJ (see figure 7). For $n = 1$, however, the MUM is very different from DVJ (see figure 6): it sits well above the low-level core, and its structure is quite similar to $n = 2$. This $n = 1$ mode does not generate a displacement of the low-level centre, and it appears that the mean state of AXI-DVJ is supercritical to all asymmetric modes. This does not necessarily imply that if 'released' into three-dimensional motions that AXI-DVJ would remain laminar and symmetric at low levels. Most likely, $n = 2$ eddies aloft would modify the flow to be more susceptible to low-level waves, and asymmetries would propagate downward.

The symmetric modes represent realizable motions of AXI-DVJ. The $n = 0$ MUM is not unstable, having a very slightly negative growth rate of -0.0033 and a decay time scale corresponding to nearly $300\tau_{circ}$, indicating that the mode is essentially neutral. This suggests that the oscillation indicated by the real and imaginary parts of the $n = 0$

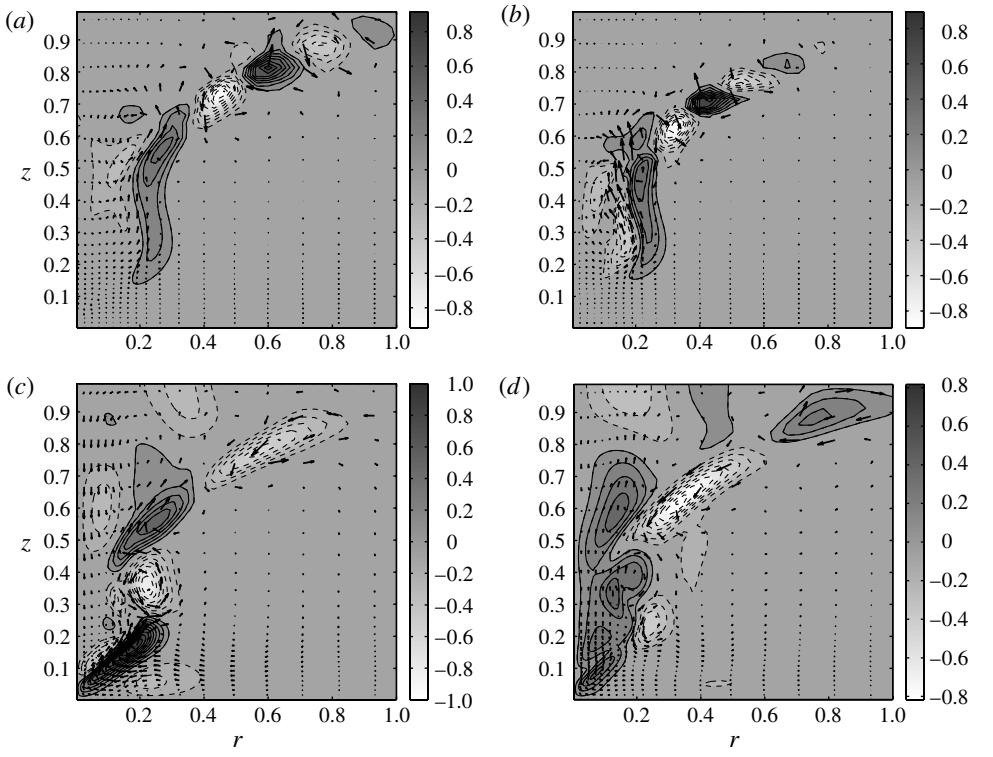

FIGURE 16. MUMs for AXI-DVJ: (*a*) real part of the MUM for $n = 1$, v_1 and $[u_1, w_1]$; (*b*) real part of the MUM for $n = 2$, v_2 and $[u_2, w_2]$; (*c*) real part of the MUM for $n = 0$, v_0 and $[u_0, w_0]$; (*d*) imaginary part of the MUM for $n = 0$. (*a*) max = 0.87, min = −0.92, int = 0.1, maxvec = 1.7; (*b*) max = 0.87, min = −0.90, int = 0.1, maxvec = 1.3; (*c*) max = 1, min = −0.80, int = 0.1, maxvec = 1.2; (*d*) max = 0.5, min = −0.82, int = 0.1, maxvec = 1.3.

MUM (see figure 16) would persist for long times, perhaps after being excited by small perturbations swept into the vortex or other nonlinear interactions. NF99*b* discussed symmetric waves propagating downward along the updraft for a very similar vortex; similar waves are present for the AXI-DVJ simulation (not shown). While the attempt of NF99*b* to reproduce these waves with a linear stability analysis was not successful, the present analysis appears to be: if we examine the evolution of the symmetric oscillations from $\mathrm{Re}\{v_0\} \to \mathrm{Im}\{v_0\} \to -\mathrm{Re}\{v_0\} \to -\mathrm{Im}\{v_0\}$, we can follow the propagation of a negative v_0 anomaly downward, from $r = 0.55$, $z = 0.75$, to $r = 0.35$, $z = 0.62$, to $r = 0.25$, $z = 0.55$, to $r = 0.2$, $z = 0.38$, and perhaps continuing into the lowest levels of the vortex.

5. Analysis of the instabilities

5.1. *Isolating the dynamics in vertically homogeneous vortices*

Of interest is the extent to which the unstable modes of a tornado-like vortex are simply modified forms of the essentially two-dimensional instabilities identified in earlier studies, or whether the horizontal shears of the vertical and radial winds are fundamental to their existence. In the next subsection, the energetics of the modes will

be computed explicitly. However, a more intuitive way to understand the dynamics of these instabilities is to simplify the basic states into flows that do not vary with height. We take radial sections of $V(r, z)$ and $W(r, z)$ selected altitudes and construct vertically homogeneous vortices with the same velocity profiles. For this exercise, the radial velocities are neglected.

The most appropriate way to solve for unstable modes on a vertically homogeneous vortex is to re-cast the linearized equations so that the perturbations are presumed to have harmonic variations in the vertical as well as azimuthal directions (e.g. Howard & Gupta 1962; Gall 1983; Leibovich & Stewartson 1983). However, to take advantage of the numerical framework already in place, an alternative approach is to change the vertical boundary conditions so that the perturbations are periodic in the vertical direction. This has some disadvantages: first, the computations are much more demanding than those which would be based on state vectors that are a function of radius only (i.e. $u_n(r)\mathrm{e}^{\mathrm{i}n\lambda+\mathrm{i}kz}$, where k is a vertical wavenumber); and second, the resulting modes must have vertical wavelengths that correspond to integer vertical wavenumbers of the domain size. To explore the dependence on vertical wavenumber it is necessary to change the domain size and repeat the computations. There are also advantages: first, it is not necessary to develop a new equation set and new discretization; and second, the instability analysis will immediately identify the vertical wavelength that is most unstable (subject to the integer wavenumber constraint). To identify the most unstable vertical wavenumber we do not have to perform stability calculations for each possible value of k.

We focus on the DVJ (figure 1*b*) and consider the flow at two altitudes, $z = 0.25$ and $z = 0.4$, where there are large radial gradients of V and W but U is nearly zero. As shown in figure 17(*a*), both profiles show local maxima in V and W, with the peaks being more prominent for $z = 0.25$. The profiles of vertical and azimuthal vorticity, shown in figure 17(*b*), have multiple changes in the signs of their gradients at both levels. Hereafter, we refer to the vortex using V only at $z = 0.25$ and $z = 0.4$ as VO25 and VO40, while the vortices using both V and W are labelled VW25 and VW40. We also show results for vortices using W only, labelled WO25 and WO40.

To perform the calculations, we used a domain with the same outer radius ($r = 2.0$) but with a vertical depth of $z = 0.5$. In preliminary tests using vertical extents of the domain ranging from 0.25 to 2.0, we found that the unstable modes typically had a vertical wavenumber of 1. Therefore we chose a vertical depth that results in a modal structure that has a similar vertical depth to the modes identified in the previous stability analyses. In particular, the MUM for $n = 2$ for the DVJ vortex has a vertical wavelength of approximately 0.5 (see figure 7*a*). The computational grid uses the same 81 stretched grid points in the radial direction as in the previous calculations. In the vertical direction 41 evenly spaced points are used. The eddy viscosity is set throughout the domain to the low-level value $\nu = 0.0004$ used in the DVJ simulation.

Figure 17(*c*) shows the growth rates for the MUMs for the VW25, VW40, VO25, VO40, WO25 and WO40 vortices. These growth rates can be compared to those shown for the DVJ vortex in figure 3. It is evident that the VW vortices are much more unstable than the VO vortices. For the VO vortices, only $n = 1$ and $n = 2$ have growth rates comparable to the DVJ vortex. The VW vortices have unstable modes out to and beyond $n = 8$. The fastest growth rates for VW25 and VW40 occur for $n = 3$ to $n = 5$ and are about twice as fast as the MUMs of the DVJ vortex. This is not surprising, since the modes in the periodic vortices are not restricted by the finite vertical extent of the strongly sheared regions or the presence of boundaries.

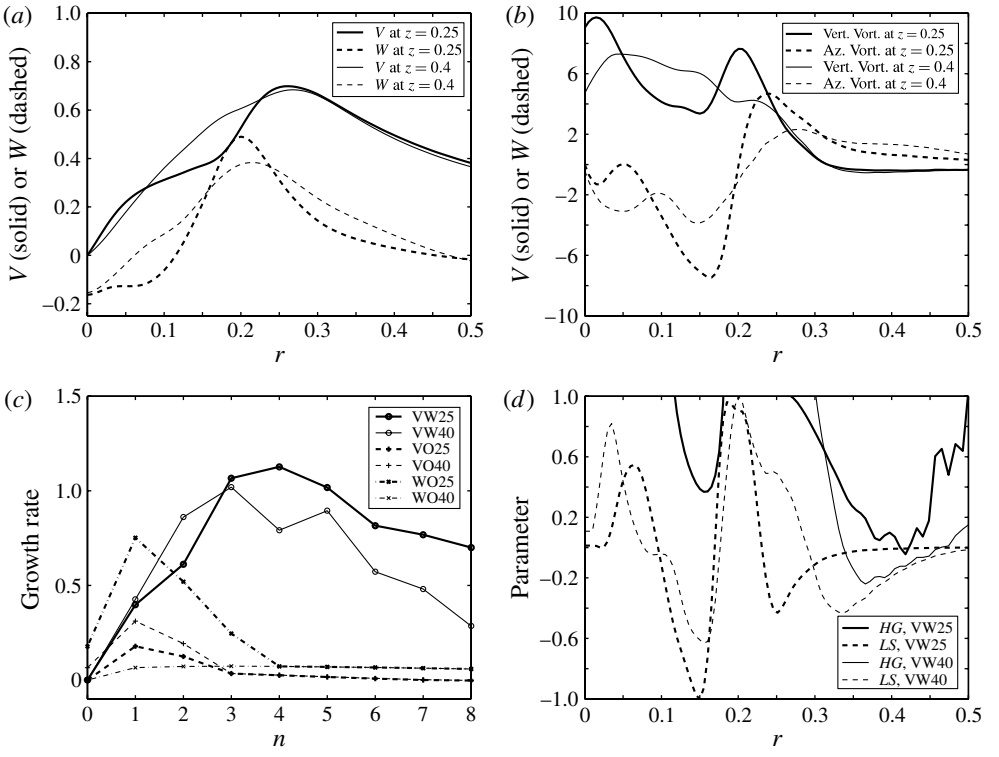

FIGURE 17. Analysis of vertically homogeneous vortices: (*a*) profiles of azimuthal and vertical wind in the DVJ at $z = 0.25$ and $z = 0.4$; (*b*) profiles of vertical and azimuthal vorticity at the same levels. (*c*) Growth rates as a function of wavenumber for the MUMs using either only the azimuthal wind (VO25 and VO40), the vertical wind (WO25 and WO40), or both the vertical and azimuthal wind (VW25 and VW40) at $z = 0.25$ and $z = 0.40$. (*d*) Stability parameters HG (equation (5.1)) and LS (equation (5.2)) for the VW25 and VW40 vortices.

Some guidance on when to expect instability in a vortex with axial flow is provided by two classic papers. Howard & Gupta (1962) derived a sufficient condition for the *stability* of a vortex to symmetric perturbations:

$$\frac{(1/r^3)(\partial \Gamma^2/\partial r)}{(\partial W/\partial r)^2} \geqslant \frac{1}{4}, \tag{5.1}$$

where $\Gamma = rV$ is the basic-state circulation, while Leibovich & Stewartson (1983; see also Emanuel 1984) derived a sufficient condition for *instability* to asymmetric perturbations:

$$V\frac{\partial \Omega}{\partial r}\left[\frac{\partial \Omega}{\partial r}\frac{\partial \Gamma}{\partial r} + \left(\frac{\partial W}{\partial r}\right)^2\right] < 0, \tag{5.2}$$

where here $\Omega = V/r$ is the basic-state angular velocity. Both of these conditions were derived assuming inviscid dynamics, and the Leibovich & Stewartson condition is only formally valid for asymmetries with large azimuthal and vertical wavenumber. Figure 17(*d*) shows radial profiles for the VW25 and VW40 vortices of the two

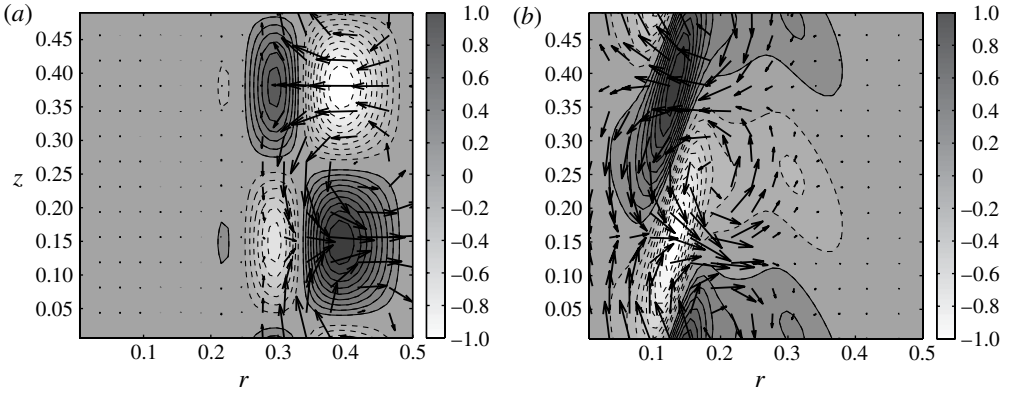

FIGURE 18. Two of the $n = 0$ unstable modes from the calculations using vertically homogeneous vortices and periodic boundary conditions: structure of the $n = 0$ mode v_0 and $[u_0, w_0]$ for (*a*) the VO40 vortex and (*b*) the WO25 vortex. (*a*) max = 1, min = −1, int = 0.1, maxvec = 3.1; (*b*) max = 1, min = −1, int = 0.1, maxvec = 7.8.

expressions (5.1) and (5.2), hereafter referred to as *HG* and *LS*, respectively. *HG* falls below 1/4 for both vortices in approximately the region $0.3 < r < 0.5$. *LS* falls below 0 in two regions for both vortices, each on either side of their respective $W(r)$ maxima near $r = 0.2$.

Despite the violation of the sufficient condition for stability to symmetric modes, neither the VW25 or the VW40 vortex profiles are unstable for $n = 0$. More interestingly, we see that only the VO40 and WO25 vortices have unstable $n = 0$ modes, while their counterparts VO25 and WO40 do not. (The *HG* condition is not well-posed for vortices without meaningful values of both V and W.) Figure 18 shows that the vertical structures of the $n = 0$ instabilities for VO40 and WO25 are quite different. The eigenvalue of the VO40 mode is real, indicating a stationary overturning circulation. To understand why VO40 has an $n = 0$ instability while VO25 does not, we can compare their profiles of azimuthal velocity and vertical vorticity (the thick solid lines in figure 17*a,b*). Beyond $r = 0.25$ V decays a bit more quickly for $z = 0.40$ than for $z = 0.25$. In fact, both of these V profiles decay slightly faster than $1/r$, indicating the presence of negative basic-state vorticity as can be seen in figure 17(*b*). However, when accounting for the contribution of the Coriolis parameter ($f = 0.2$), only the $z = 0.4$ profile contains a small area of negative absolute vertical vorticity $\eta = \zeta + f$ in the range $0.34 < r < 0.48$ with a minimum value of $\eta = -0.14$. Negative η indicates the possibility of purely inertial instability, and this explains the appearance of the symmetric mode for VO40 and the absence of a similar mode for VO25.

The WO25 symmetric unstable mode comes as a conjugate pair that is shifted by 1/4-wavelength in the vertical, indicating that it is propagating upward with time. Another feature is that its overturning circulation is ∼8 times stronger than the azimuthal circulations. In fact, given that the basic state for this mode is an axial jet with no azimuthal flow, one might wonder why or even how this mode should contain any azimuthal motion at all. These motions come from the Coriolis force inherited from the underlying equations of F09. To assess the effect of f on the stability of WO25, the stability analysis was repeated for $f = 0$. Remarkably, the growth rates and structures were very similar for every wavenumber, indicating that background rotation

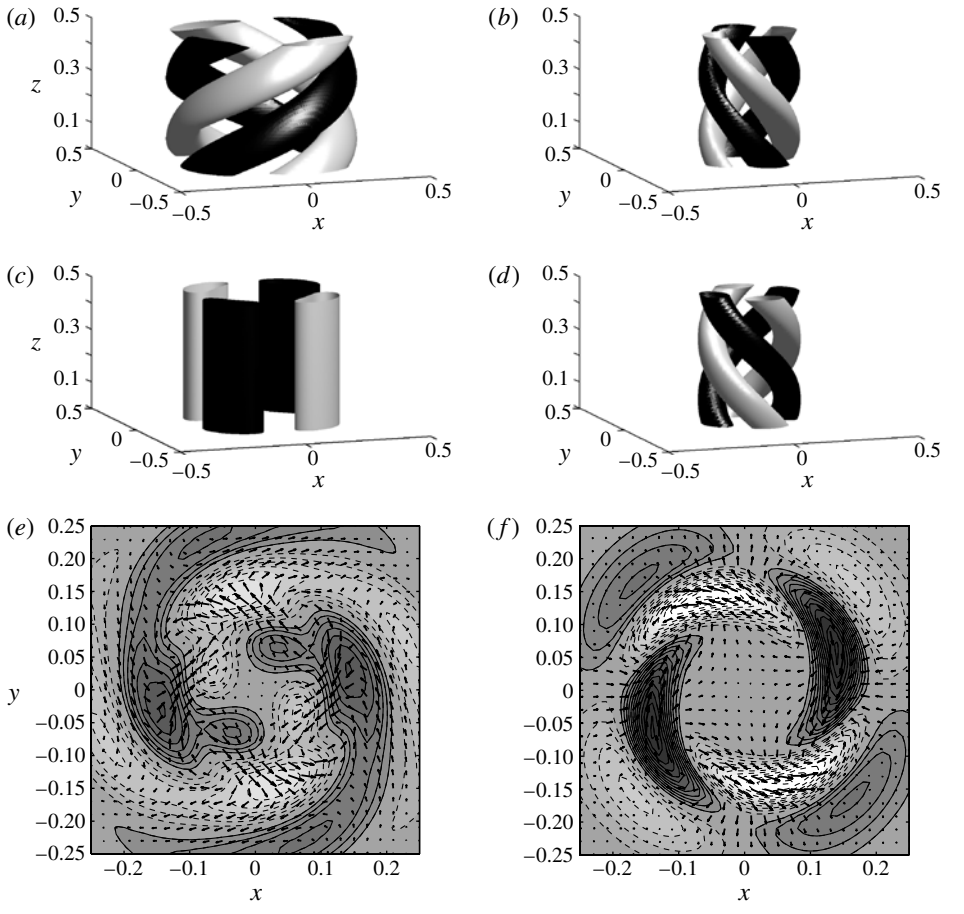

FIGURE 19. Structures of the $n = 2$ unstable modes for the vertically homogeneous vortices: (*a*) isosurface of perturbation pressure $= \pm 1.1 \times 10^{-1}$ for the MUM for VW25 ; (*b*) for the second MUM of VW25 ($\pm 8 \times 10^{-3}$); (*c*) MUM for VO25 ($\pm 1.3 \times 10^{-1}$); (*d*) MUM for WO25 ($\pm 5.8 \times 10^{-2}$). (*e*) Horizontal section at $z = 0.24$ of vertical velocity (contours) and horizontal velocity (vectors) for the second MUM of VW25 (shown in *b*); (*f*) for the MUM for WO25. (*e*) max $= 0.71$, min $= -0.71$, int $= 0.10$, maxvec $= 1.30$; (*f*) max $= 1.23$, min $= -1.23$, int $= 0.10$, maxvec $= 1.08$.

has a very small effect on the dynamics of inner-core instabilities. The structure of the MUM for $n = 0$, WO25, and $f = 0$ is nearly identical to that shown for $f = 0.2$ (figure 18*b*) but with the azimuthal velocities exactly equal to zero (not shown).

Turning to the asymmetric modes, we first consider the MUM for $n = 2$ for VW25. A rendering of its perturbation pressure is shown in figure 19(*a*). The mode consists of an overturning circulation with vortex lines, and lines of constant phase, that spiral counterclockwise in the upward direction, roughly parallel with the total vorticity vector of the basic-state flow on the *outside* of the updraft maximum. This suggests that the mode is of the type previously identified by Leibovich & Stewartson (1983) and Emanuel (1984), located on the outside edge of the axial updraft where the azimuthal vorticity is positive and the inertial stability is weak. Similar modes have been identified in numerical simulations and stability analyses

of vortex breakdown in rotating-lid experiments (Serre & Bontoux 2002; Gallare & Chomaz 2003; Oberleithner *et al.* 2011). However, it is hard to see how a mode of this type could exist in the DVJ. All the unstable modes identified by stability analyses of the OCV, DVJ and TCV spiral in the opposite direction, as would seem necessary given the rapid decrease with height of $V(r, z)$.

While the non-dimensional growth rate for this mode is 0.61, it happens in this case that the second MUM is nearly as strong with a growth rate of 0.55. As shown in figure 19(*b*), the structure of this mode is quite different, spiralling clockwise in the upwards direction and at a much smaller angle relative to the vertical. The mode exists at a smaller radius, indicating that it is associated with wind shear on the *inside* of the updraft. As shown in figure 17(*d*), the *LS* sufficient condition for instability is met on the inside of the updraft, where not only is $\partial W/\partial r$ significant, but $\partial \Omega/\partial r$ is also locally negative (not shown) due to a local dip in the $V(r)$ profile around $r = 0.2$. In this sense, this mode is rather different from the ones originally envisioned by Leibovich & Stewartson (1983) for trailing vortices with axial wind profiles that decrease monotonically from $r = 0$. Remarkably, their instability condition identifies the location of these modes just as well.

Also shown in figure 19 are renderings of perturbation pressure for the MUMs of VO25 and WO25. The MUM for VO25 is completely two-dimensional, while the structure of the MUM for WO25 is remarkably similar to that of VW25. The strong similarities in the structures of the second mode for VW25 and first mode for WO25 suggest that one of these modes could be an idealization of the $n = 2$ mode for the DVJ vortex that encapsulates the mechanism of its instability. However, the details of their inner-core flow structures, as shown in figure 19(*e*,*f*), do not compare well with the structures of the $n = 2$ mode of the DVJ vortex as shown in figure 7. At first, figure 19(*e*) might appear very similar to figure 7(*c*), but closer inspection shows that the relative orientations of the phase-shifted waves is opposite between the two cases.

All the asymmetric modes for VW40 are similar in structure to the mode in figure 19(*a*), suggesting these also would not be viable mechanisms for instability in the DVJ vortex. For $n > 2$, the MUMs for VW25 were higher-wavenumber versions of the second MUM for $n = 2$ (figure 19*b*). If these modes are indeed viable in an environment of negative $\partial V/\partial z$, the results suggest that the DVJ vortex should be unstable to higher wavenumbers. Instead the growth rates cut off sharply for $n > 3$ (figure 3). An explanation for the high-wavenumber cutoff could stem from the vertical propagation speeds of these waves. As these waves spiral clockwise in the upward direction, their phase lines should propagate upward as the modes turns counterclockwise (cyclonically), and indeed all the modes for VW25 for $n = 2$ to $n = 6$ were found to have fast upward phase speeds. To identify the actual propagation of the modes requires the group velocity. While our numerical method does not specify vertical wavenumber, the wavenumbers can be changed by adjusting the vertical extent of the periodic domain. Group velocities were computed for the 'inner' modes (as shown in figure 19*b*) by finite-differencing their eigenvalues for domains of different vertical length $L_z = 0.5$ and $L_z = 0.55$, i.e. approximating $\partial\omega/\partial k = \Delta\omega/\Delta k$, where $k = 2\pi/L_z$. The vertical group velocities for the inner modes for $n = 2$ to $n = 6$ turn out to be positive but quite small, with values of 0.078, 0.080, 0.082, 0.096 and 0.117, respectively. This shows that the modes remain nearly stationary relative to the vertical flow, which is consistent with the fact that these modes straddle the location where $W(r) = 0$. There is a small increase in upward group speed with wavenumber, consistent with the notion that the higher wavenumbers would not be able to remain

embedded in the strongest part of the updraft, but the increase is very small and this does not offer a robust explanation for why the DVJ is increasingly stable for $n > 2$. Nonetheless, we did find previously that the physical location of the MUMs in the DVJ vortex does shift upward for $n = 1$, 2 and 3 (see figures 6 and 7; $n = 3$ not shown), consistent with the hypothesis that the flow in the most unstable region is supercritical for higher wavenumber modes.

5.2. *Wave–mean flow interactions and energetics*

For effectively two-dimensional flows perhaps the easiest way is to interpret the structure and growth of an unstable mode is in terms of vorticity perturbations that 'live' along vorticity gradients and amplify each other through their induced circulations. However, the previous results suggest that for vortices with strong radial and vertical circulations the dynamics of their instabilities are not so easily interpreted. Another way to understand an instability is to consider the way in which it interacts with the basic state. An asymmetric wave interacts with the symmetric flow via azimuthally averaged eddy fluxes. For incompressible flow in cylindrical coordinates, these can be diagnosed as:

$$\frac{\partial \overline{u}}{\partial t} = \cdots - \frac{1}{r}\frac{\partial}{\partial r}\overline{(ru'^2)} - \frac{\partial}{\partial z}\overline{(u'w')} + \frac{\overline{(v'v')}}{r} = \cdots + \dot{\overline{u}}_{efd}, \tag{5.3}$$

$$\frac{\partial \overline{v}}{\partial t} = \cdots - \frac{1}{r^2}\frac{\partial}{\partial r}\overline{(r^2u'v')} - \frac{\partial}{\partial z}\overline{(v'w')} = \cdots + \dot{\overline{v}}_{efd}, \tag{5.4}$$

$$\frac{\partial \overline{w}}{\partial t} = \cdots - \frac{1}{r}\frac{\partial}{\partial r}\overline{(ru'w')} - \frac{\partial}{\partial z}\overline{(w'^2)} = \cdots + \dot{\overline{w}}_{efd}, \tag{5.5}$$

where we have left out the advection and pressure force terms $(\cdots)$ that complete the equations and the terms $\dot{\overline{u}}_{efd}$, $\dot{\overline{v}}_{efd}$ and $\dot{\overline{w}}_{efd}$ represent the tendencies due to the eddy-flux divergences. Here, the bars over the un-primed variables refer to the azimuthal-mean flow (note that here we do not restrict ourselves to the basic-state flows U, V and W, since (5.3)–(5.5) are valid for time-evolving azimuthal-mean circulations and also for large-amplitude asymmetries), while the bars over the products of primed variables refer to azimuthal-mean eddy correlations.

Figure 20 shows the eddy-flux tendency on the symmetric flow caused by the $n = 1$ and $n = 2$ MUMs for the OCV. For $n = 1$, the eddy tendencies show large accelerations of the azimuthal and vertical winds near the centre axis. This is a typical tendency structure for $n = 1$ perturbations which can be better interpreted as a displacement of the vortex centre: when the vortex is displaced off its original axis, the azimuthal-mean v and w velocities at smaller radius (relative to the original axis) increase. For $n = 2$, the azimuthal tendencies have the effect of locally intensifying the wind field along $r = 0.12$ between $z = 0.3$ and $z = 0.5$, while decelerating the flow along $r = 0.06$ in the same range. The eddy tendencies on u and w appear to force outward and downward motion and upward and inward motion where the v tendencies are positive and negative, respectively, but the physical effects of these are difficult to interpret. (Unlike forcings on the azimuthal wind, forcings on the meridional flow $[u, w]$ are subject to the incompressibility constraint. To the extent that this forcing is divergent in the r–z plane, pressure forces would appear to exactly cancel such motions. Thus it is virtually impossible to decipher the effects of these forcings on the symmetric mean flow without additional calculations with a symmetric model.) In general, it appears that this $n = 2$ mode acts to redistribute the small local maximum in V near $r = 0.1$, $z = 0.35$ (see figure 1*a*).

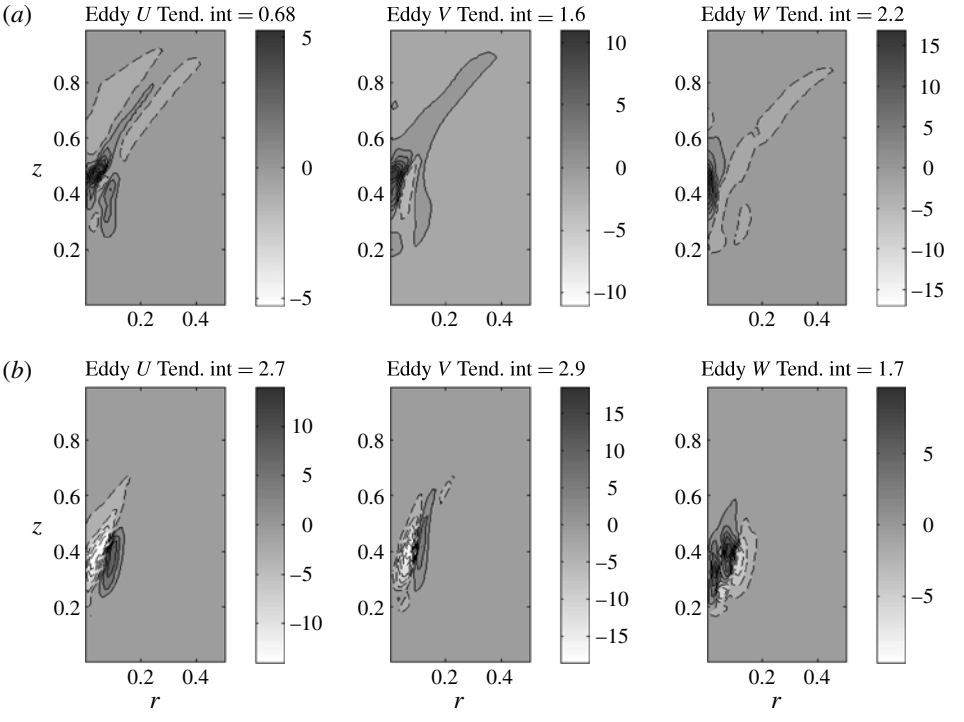

FIGURE 20. Eddy-flux tendencies for U, V, W (from left to right) from the MUMs for the OCV for (*a*) $n = 1$ and (*b*) $n = 2$. The contour intervals are indicated at the top of each plot, and the shading range is centered on zero and extends from negative to positive of the absolute value of the maximum or minimum value, whichever is larger.

Figure 21 shows eddy-flux tendencies for the DVJ. The $n = 1$ mode also acts to accelerate the low-level flow radially inward of the low-level jet, again consistent with a growing displacement of the low-level circulation. For $n = 2$ the azimuthal tendencies are trying to reshape $V(r, z)$ by 'filling in' the low-velocity notch around $r = 0.25$, $z = 0.25$, while the eddy tendencies on u and w around this location are again outward/downward and inward/upward. Further aloft, the eddy tendencies appear to be accelerating the relatively quiescent flow inside the outflow jet.

Figure 22 shows the eddy tendencies for the MUM for $n = 2$ and $n = 3$ for the TCV. For both wavenumbers, all three eddy tendencies show acceleration of the flow radially inward and above the radial outflow jet that emanates from the origin to near $r = 0.2$, $z = 0.1$ (see figure 1*c*). These unstable modes are working to 'spin up' the relatively motionless region just inside the region of peak winds.

What influence do these modes have on the mean flows of the tornado-like vortices? The differences in structure between DVJ and AXI-DVJ indicate that asymmetries and their eddy tendencies do indeed change the mean flow. If we presume that the rate of change of the temporal-azimuthal mean is zero, we can diagnose the mean eddy tendencies as the residual of the momentum equation for symmetric motions:

$$-\dot{\bar{v}}_{efd} = -U\left(\frac{\partial V}{\partial r} + \frac{V}{r} + f\right) - W\frac{\partial V}{\partial z} + \nu\left[\frac{\partial}{\partial r}\left(\frac{1}{r}\frac{\partial}{\partial r}(rV)\right)\right] + \nu\frac{\partial^2 V}{\partial z^2} + \frac{\partial \nu}{\partial z}\frac{\partial V}{\partial z} \quad (5.6)$$

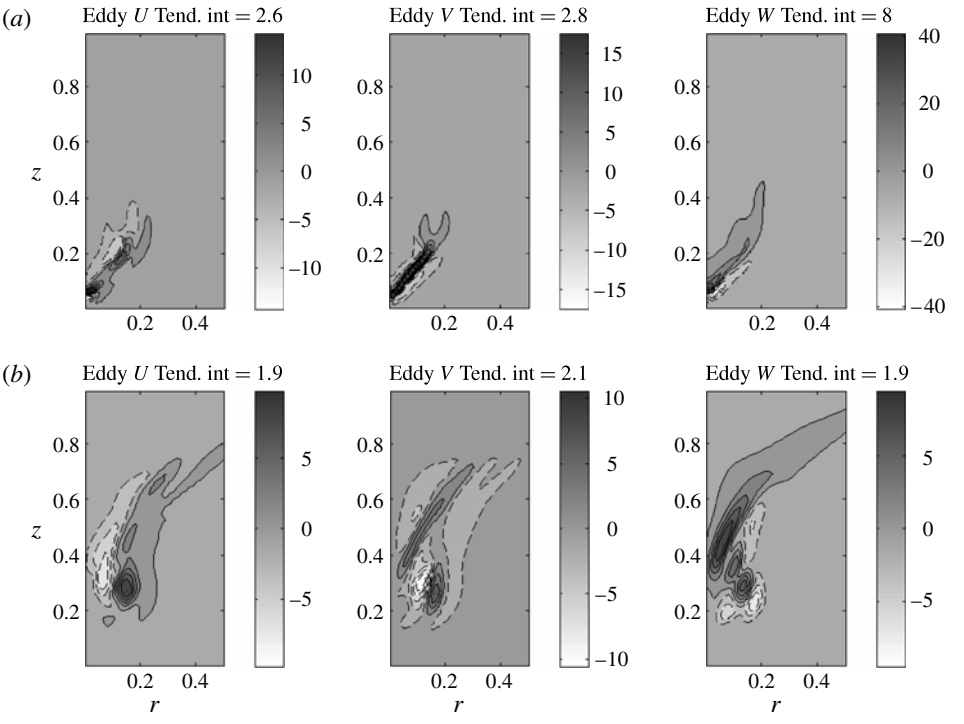

FIGURE 21. As in figure 20, but for the DVJ.

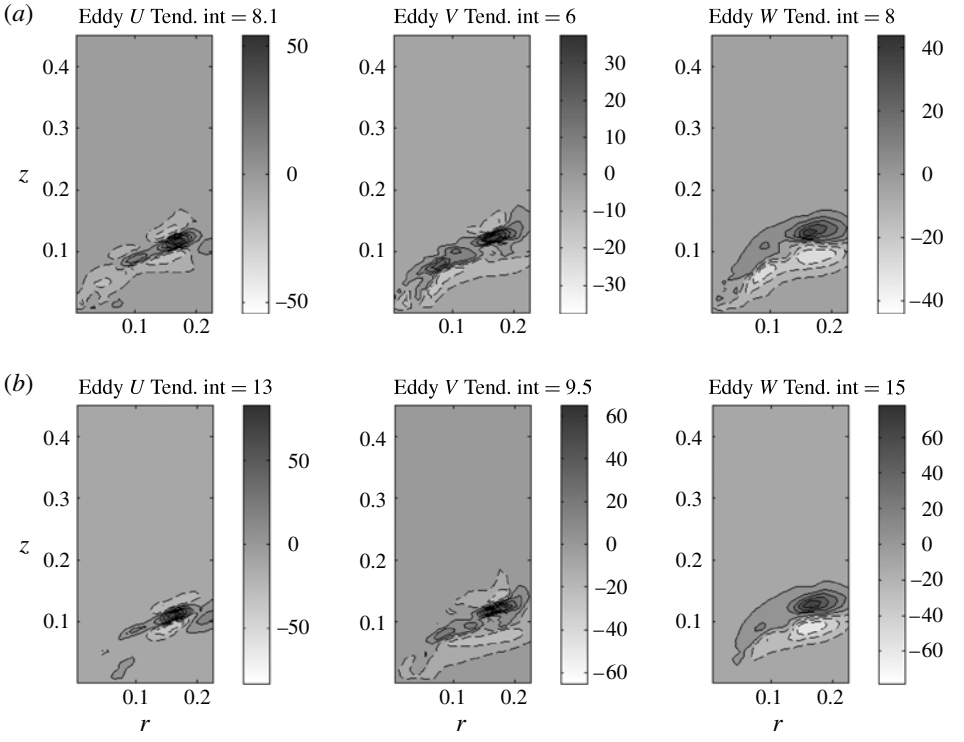

FIGURE 22. As in figure 20, but for the TCV, for (*a*) $n = 2$ and (*b*) $n = 3$.

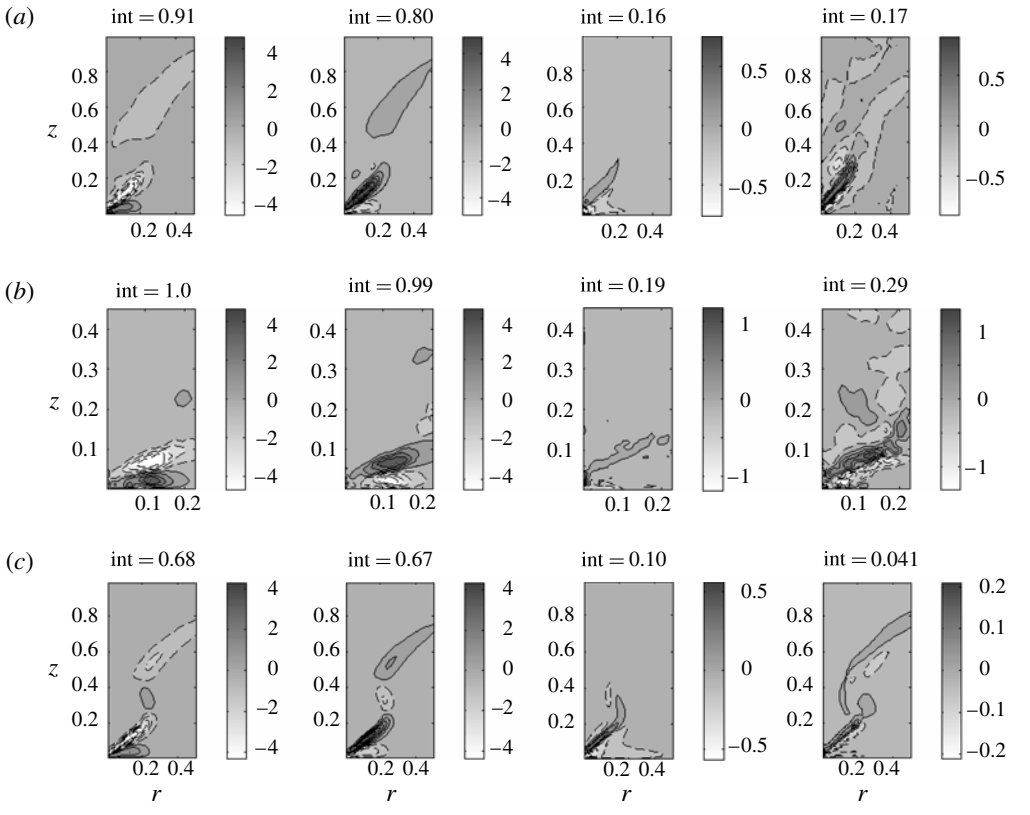

FIGURE 23. Symmetric advective and diffusive tendencies from (5.6) and their residuals (from left to right: radial V advection, vertical V advection, frictional V tendency and negative of residuals), computed for the time-mean flows for (*a*) the DVJ, (*b*) the TCV and (*c*) the AXI-DVJ, with labels and shading as in figure 20.

where here we have assumed that the viscosity ν only varies in the z-direction. Figure 23 shows each of the terms on the right-hand side of (5.6) and the negative of the resulting residuals for DVJ, TCV, and AXI-DVJ. For the first two cases, the residuals are significant, with peak values 20–30 % of the peak values of advection. At some locations above the corner flow region, the residuals are about half as large as the advective tendencies.

If one compares the structure of the negative residual for the DVJ to the plots of $\dot{\overline{v}}_{efd}$ for $n = 1$ and $n = 2$ (figure 21), it is apparent that the residual contains structures that are similar to $\dot{\overline{v}}_{efd}$ for each wavenumber. There is an axis of positive tendency emanating upward from the origin that matches $\dot{\overline{v}}_{efd}$ for $n = 1$, and there is a local negative maximum in tendency near $r = 0.1$, $z = 0.3$ that closely matches a similar feature in the eddy tendency for $n = 2$. In other words, the residuals of the symmetric momentum equation diagnosed from (5.6) are fairly well approximated by a linear combination of the eddy tendencies of the two most unstable modes. Similarly, it is not hard to see the negative residual for the TCV as some combination of $\dot{\overline{v}}_{efd}$ for $n = 2$ and $n = 3$ as shown in figure 22.

Interestingly, the residuals for AXI-DVJ are much smaller, being less than the advective tendencies by more than one order of magnitude. In other words, the time mean of the symmetric simulation is quite close to being a steady solution of the symmetric equations.

5.3. *Energetics of the unstable modes*

A more comprehensive way to analyse the interaction between an instability and its basic state is in terms of the exchange of energy between the basic-state flow and the growing perturbations. As discussed in WG84 and Nolan (2005*a*), for three-dimensional asymmetric perturbations to a symmetric vortex an equation may be derived for the rate of change of total perturbation kinetic energy (KE):

$$\frac{\partial E'}{\partial t} = -\iint \left\{ \left[\overline{u'v'} \left(\frac{\partial \overline{v}}{\partial r} - \frac{\overline{v}}{r} \right) \right]_{vr} + \left[\overline{u'w'} \frac{\partial \overline{w}}{\partial r} \right]_{wr} + \left[\overline{u'u'} \frac{\partial \overline{u}}{\partial r} + \overline{v'v'} \frac{\overline{u}}{r} \right]_{ur} + \left[\overline{v'w'} \frac{\partial \overline{v}}{\partial z} \right]_{vz} + \left[\overline{w'w'} \frac{\partial \overline{w}}{\partial z} \right]_{wz} + \left[\overline{u'w'} \frac{\partial \overline{u}}{\partial z} \right]_{uz} + [\overline{u'F'_r} + \overline{v'F'_\lambda} + \overline{w'F'_z}]_F \right\} 2\pi r \, \mathrm{d}r \, \mathrm{d}z. \tag{5.7}$$

The F terms refer to the frictional tendencies on u, v and w, respectively. The terms have been grouped into brackets and labelled. Except for the frictional term, each of these terms represents an eddy flux across a shear. Generally, growth in perturbation KE occurs when the eddy fluxes transport momentum from a faster part of the mean flow to a slower part. As a result, the kinetic energy of the mean flow decreases, and the eddy energy grows correspondingly. Each of the integrands in (5.7) can be computed locally and volume integrated to get the total contribution from each term to the energy growth.

However, a more physically intuitive form of this equation can be obtained by integrating each of the eddy-flux terms by parts. Alternatively, the same equation can be found by starting from the full equations for the symmetric motions as in (5.3)–(5.5), multiplying each by $\bar{u}$, $\bar{v}$ and $\bar{w}$, summing the equations and integrating. This gives an equation for the kinetic energy of the symmetric flow, which must be balanced by the gain or loss of eddy energy, except for the eddy friction terms, which can be carried over from (5.7). Thus the alternative form is:

$$\frac{\partial E'}{\partial t} = \iint \left\{ \left[\overline{v} \frac{1}{r^2} \frac{\partial}{\partial r} \overline{(r^2 u'v')} \right]_{vr} + \left[\overline{w} \frac{1}{r} \frac{\partial}{\partial r} \overline{(ru'w')} \right]_{wr} + \left[\overline{u} \left(\frac{\partial}{\partial r} \overline{(u'u')} + \frac{\overline{v'v'}}{r} \right) \right]_{ur} + \left[\overline{v} \frac{\partial}{\partial z} \overline{(v'w')} \right]_{vz} + \left[\overline{w} \frac{\partial}{\partial z} \overline{(w'w')} \right]_{wz} + \left[\overline{u} \frac{\partial}{\partial z} \overline{(u'w')} \right]_{uz} + [\overline{u'F'_r} + \overline{v'F'_\lambda} + \overline{w'F'_z}]_F \right\} 2\pi r \, \mathrm{d}r \, \mathrm{d}z. \tag{5.8}$$

The integrands in (5.7) and (5.8) are not pointwise equal and the term-by-term equality only comes after volume integration over the domain. This latter form of the equation is more intuitive because, as will be shown below, plotting the spatial structure of each term also shows where and in what sense the eddies are changing the basic-state flow.

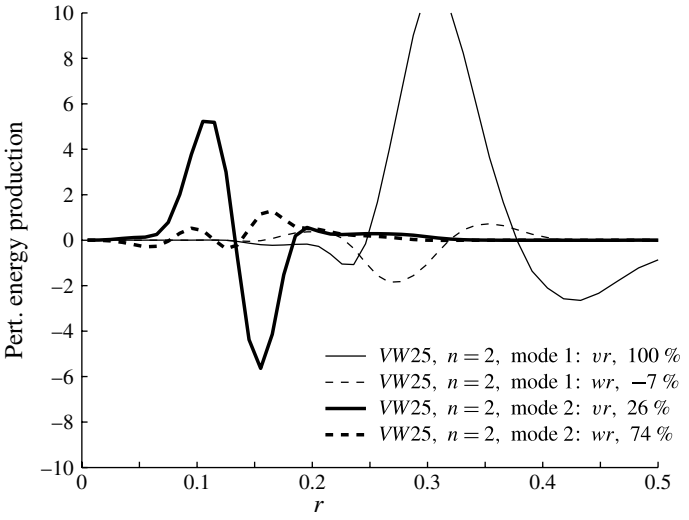

FIGURE 24. Energy exchange terms for the first two MUMs for $n = 2$ in the VW25 vortex.

Before proceeding to the energetics of instabilities in the tornado-like vortices, we briefly discuss the energy exchange terms for some of the modes from the vertically homogeneous vortices above. For these only the vr, wr, and frictional terms are non-zero. Recalling that they seemed to capture two distinct dynamical growth mechanisms in the DVJ, we consider the first MUM and the second MUM for $n = 2$ in the VW25 vortex as shown in figure 19(*a,b*). Figure 24 shows radial profiles of the vr and wr terms for these modes. The percentages in the legend show the fraction of the total positive energy contribution that comes from each term.

The first MUM exists at larger radius and gains all of its energy from the vr term. The wr term acts to only slightly dampen the growth rate. The instability works to decelerate V around $r = 0.3$ and to accelerate V around $r = 0.425$, thereby 'flattening' the wind profile outside the RMW and thus increasing the inertial stability there. The mode also works to increase w around $r = 0.275$ and decrease it around $r = 0.35$, perhaps shifting the largest negative values of $\partial W/\partial r$ to larger radii.

As expected, the dynamics of the second MUM are quite different. This mode gains 74 % of its energy from the wr term and just 26 % from the vr term. While larger in amplitude the oppositely signed peak values of the vr term evidently cancel each other when integrated. The second mode works to accelerate V near $r = 0.15$ and decelerate it near $r = 0.1$, thereby bringing $V(r)$ closer to solid-body rotation. This mode also works to make W less negative near $r = 0.1$ and less positive near $r = 0.17$, leading to a weaker gradient of W.

Returning to the vortices of F09, it would take far too much space to show all seven terms for the many modes that we have discussed, so we will discuss the energetics of selected MUMs for each case: $n = 1$ for the OCV, $n = 2$ for the DVJ vortex, and $n = 2$ for the TCV. Table 1 summarizes the numerical values of the energy exchange terms for each of these modes. Each mode is normalized as above so that the peak perturbation azimuthal wind is equal to 1. The last two rows of each column show the total energy conversion computed from summing the exchange terms in (5.8) and the rate of energy increase predicted by the growth rate, $\mathrm{d}E'/\mathrm{d}t = 2s_r E'$. The close matches

Energy conversion term:	Mode:		
	$n = 1$, OCV	$n = 2$, DVJ	$n = 2$, TCV
ur	−0.34 (−15 %)	−0.61 (−12 %)	−0.56 (−14 %)
uz	0.02 (−0.01 %)	0.05 (1 %)	0.57 (14 %)
vr	0.03 (1.4 %)	0.003 (0.07 %)	−0.02 (−0.6 %)
vz	0.29 (13 %)	0.69 (14 %)	1.88 (47 %)
wr	0.70 (31 %)	2.16 (44 %)	−0.03 (−0.06 %)
wz	1.27 (55 %)	1.98 (41 %)	1.55 (39 %)
F	−0.74 (−32 %)	−2.07 (−42 %)	−0.82 (−21 %)
Total	1.21	2.21	2.57
Predicted	1.27	2.23	2.45

TABLE 1. Energy conversion terms ($\times 10^{-2}$) for some of the most unstable modes. Fraction of total positive conversion is shown in brackets.

in these values indicates that the energy calculations are consistent. Values computed from (5.7) agreed within a few per cent for each term (not shown). Also shown are the percentage contribution that each conversion term makes relative to the total positive conversion, i.e. the ratio between that term and the sum of all the positive terms.

Table 1 shows that the radial shear of azimuthal wind (the vr term) plays a very small role in the dynamics of the unstable modes for all three vortices. The wr term is significant for the MUMs for the OCV and DVJ, contributing 31 % and 44 %, respectively, of the perturbation kinetic energy production. The term which is consistently significant for all three modes is the wz term, contributing 55 %, 41 % and 39 % of the energy production in the OCV, DVJ and TCV, respectively.

Thus we find that the consistently important physical process for the growth of asymmetric modes in tornado-like vortices is the eddy tendency of vertical velocity perturbations to accelerate or decelerate the basic-state vertical velocity. For the OCV and DVJ, the wr term is also significant, while for the TCV, it is the vz term that is also significant. The spatial structures of the top two positive energy production terms for each of the three vortices are shown in figure 25. Where these terms are positive, the growing unstable modes are acting to decelerate the basic-state flow, and they act to accelerate the basic state where these terms are negative.

For the $n = 1$ mode of the OCV, the largest energy conversions come from deceleration of the basic-state vertical flow along the centre axis and in the upper outflow region. However, the $n = 1$ mode primarily represents a displacement of the vortex off its centre axis, and the energy exchanges are simply those which are consistent with such displacements, such that some of the symmetric flow projects onto $n = 1$ asymmetries and increases the asymmetric energy.

For the DVJ, the $n = 2$ mode grows primarily by decelerating the vertical updraft that lies along $r = 0.18$ in the range $0.2 < z < 0.4$, through both radial and vertical eddy fluxes. To some extent, the positive tendencies of the wr term are being diminished by the localized area of negative tendencies of the wz term.

For the TCV, the $n = 2$ mode grows primarily by decelerating the intense azimuthal and vertical flows that lie along the radial outflow jet directly above the low-level wind maximum. Both the vz and wz terms are acting to displace the jet upward, as indicated by the eddy tendencies in figure 22. As reported in table 1, the uz term is the third

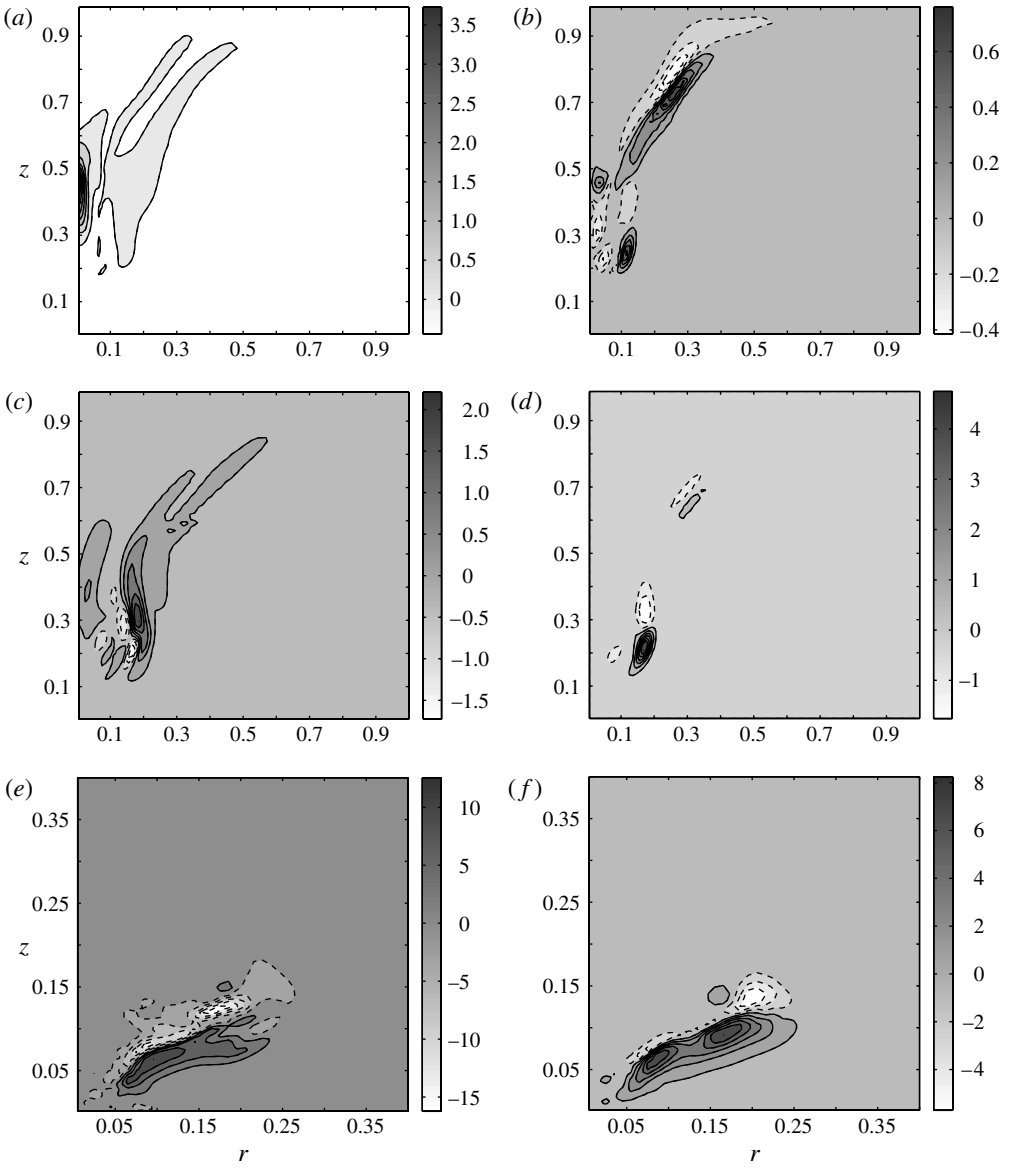

FIGURE 25. The top two energy production terms for MUMs from each vortex: (*a*) *wr* term (31 % of total positive perturbation energy production), and (*b*) wz term (55 %) for the $n = 1$ MUM for the OCV; (*c*) wr (44 %) and (*d*) wz (41 %) terms for the $n = 2$ MUM for the DVJ vortex; (*e*) *vz* (47 %) and (*f*) *wz* (39 %) terms for the $n = 2$ MUM for the two-celled vortex. Units are arbitrary but consistent among the plots, as each mode has been normalized to have a peak azimuthal wind perturbation of 1.0. (*a*) max = 3.73, min = −0.44, int = 0.46; (*b*) max = 0.76, min = −0.42, int = 0.13; (*c*) max = 2.21, min = −1.73, int = 0.44; (*d*) max = 4.75, min = −1.76, int = 0.72; (*e*) max = 1.26, min = −0.16, int = 3.20; (*f*) max = 8.25, min = −5.71, int = 1.55.

largest contributor, and it is also associated with an upward spreading of the outflow jet (not shown).

6. Summary and conclusions

The multiple vortex phenomenon has been well documented in tornado-like vortices of all scales, from laboratory vortices on the scales of centimetres to large tornadoes on the scales of hundreds of metres. From their earliest recognition, multiple vortices have been presumed to arise from dynamical instability of the tornado-like vortex (Ward 1972; Davies-Jones 1973). However, the lack of dynamical consistency between the basic states previously used for linear stability analysis and the dynamics of real tornado-like vortices has left some doubt as to whether prior results and interpretations would apply to more realistic tornado-like vortices. In this study, linearized stability analyses have been performed for basic-state flows that are more consistent with real tornado-like vortices, most especially in regard to the presence of a frictional boundary layer and strong low-level inflow.

The linear stability analyses correctly predict the wavenumber of the dominant modes for each vortex and the general structures and locations of the asymmetries that result, supporting the widely held notion that the multiple vortex phenomenon is a result of fluid-flow instability. Analysis of the tendencies on the symmetric flow due to the eddy fluxes of the most unstable modes showed how these modes contribute to the mean state: the asymmetries work to 'spin up' the flow inside the vortex, bringing the flow closer to solid-body rotation. These results are consistent with the differences between the mean states generated by three-dimensional simulations and the mean state of a purely axisymmetric simulation.

However, some prior conclusions on the fundamental nature of the instabilities and the relative roles of their interactions with the radial shears of the azimuthal and vertical winds have been contradicted. The unstable modes identified here, found to bear meaningful similarities to the strong asymmetric motions in the underlying nonlinear simulations, gain a large part of their energy through eddy interactions with the vertical gradient of the vertical wind. For the OCV and DVJ, the other important term is the eddy interaction with the radial shear of the vertical wind, and for the TCV it is the vertical gradient of the azimuthal wind.

A distinctly new result is the possible contribution of global symmetric instabilities to the dynamics of tornadoes. Symmetric modes were identified for each vortex that have some similarities with symmetric oscillations observed in real tornadoes by Bluestein *et al.* (2003) and Tanamachi *et al.* (2007). While the periods of the most unstable symmetric oscillations are considerably longer than the observed periods in those two cases, the linear model also identifies less unstable (nearly neutral) modes with periods that are closer the observed oscillation periods. Another possibility is that, due to limitations in resolution and to smoothing in the analysis process, the radar observations are underestimating the azimuthal-mean winds of the tornadoes. This would mean that their circulations times (τ_{circ}) are shorter, and would bring the ratio of the observed symmetric oscillation periods to the observed circulation times more in agreement with the results here (H. Bluestein, personal communication).

It is important to discuss some caveats regarding whether the results shown here accurately depict the dynamics of the multiple vortex phenomenon in real atmospheric vortices. The underlying simulations of Fiedler (2009) that provide the basic-state flows are essentially direct-numerical-simulation (DNS) representations of

low-Reynolds-number ($Re \sim 1000$) tornado-like vortices. The simulations also use a simple no-slip lower boundary condition. In these ways, the simulations are probably closer to laboratory model simulations than to actual tornadoes which have vastly larger Reynolds numbers and often occur over rough terrain that would be better modelled with a turbulent-drag-law lower boundary condition. A linearized stability analysis of the wind field and the spatially varying effective eddy viscosity field generated from a fully three-dimensional large-eddy simulation, such as those by Lewellen *et al.* (1997, 2000), could possibly produce structures even more like those observed.

It is possible that in many real tornadoes the boundary layer is even thinner and the mass flux even smaller than what is depicted in the TCV used here. In this case, much of the swirling flow above the boundary layer might indeed be more like those simulated and analysed by Rotunno (1984) and Walko & Gall (1984). In turn, prior conclusions about the energetics and dynamics of the multiple vortices in these tornadoes – that they rely mostly on the radial shears of the vertical and azimuthal winds – could turn out to be correct for those types of vortices.

This paper has explored the extent to which the unstable modes can be understood in terms of 'classic' stability analysis of vortices with an axial jet as developed by Howard & Gupta (1962) and Leibovich & Stewartson (1983). While the *HG* necessary condition for symmetric instability is met well in some parts of the DVJ, a vertically homogeneous version of this vortex does not show symmetric instabilities, while the full version of the DVJ shows a weak symmetric instability in a region where *HG* is not satisfied. In contrast, the *LS* condition was successful in identifying where asymmetric unstable modes would occur in the vertically homogeneous vortices, including modes which are rather different in structure from the modes originally identified by Leibovich & Stewartson.

Further limitations of using the *HG* and *LS* conditions as guidance can be seen by plotting where these conditions are satisfied in the full basic-state flow fields (figure 26). Both conditions are met over large regions outside of each vortex, and yet in these areas strong symmetric or asymmetric overturnings were not observed. This could be due to the larger viscosity values ($\nu = 0.001$) in the upper part of the domain or the presence of significant radial inflow and outflow. In the TCV, fast-growing instabilities occurred for $n = 2$ and $n = 3$ in the 'corner flow region'. Yet in this region the *LS* condition is only marginally met at scattered locations. This is consistent with the fact that the MUMs for the TCV were entirely dependent on the vertical shears of U, V and W, which do not exist in the framework of columnar vortex stability analysis.

These findings simply highlight the fact that while classic vortex theory for both two-dimensional and three-dimensional flows is a useful way to begin to understand the dynamics of tornado-like vortices, the presence of large radial velocities and the very large vertical gradients of all three velocity fields precludes this theory from making complete or even accurate predictions. The tornado-like vortex is a complex circulation that involves balances between friction, momentum transport, eddy fluxes, and large non-hydrostatic pressure gradients. Any analysis, linear or nonlinear, should treat it as single, complex entity.

Acknowledgements

The author would like to thank Professor B. Fiedler for providing the temporally and azimuthally averaged wind fields and a subset of the model output from his

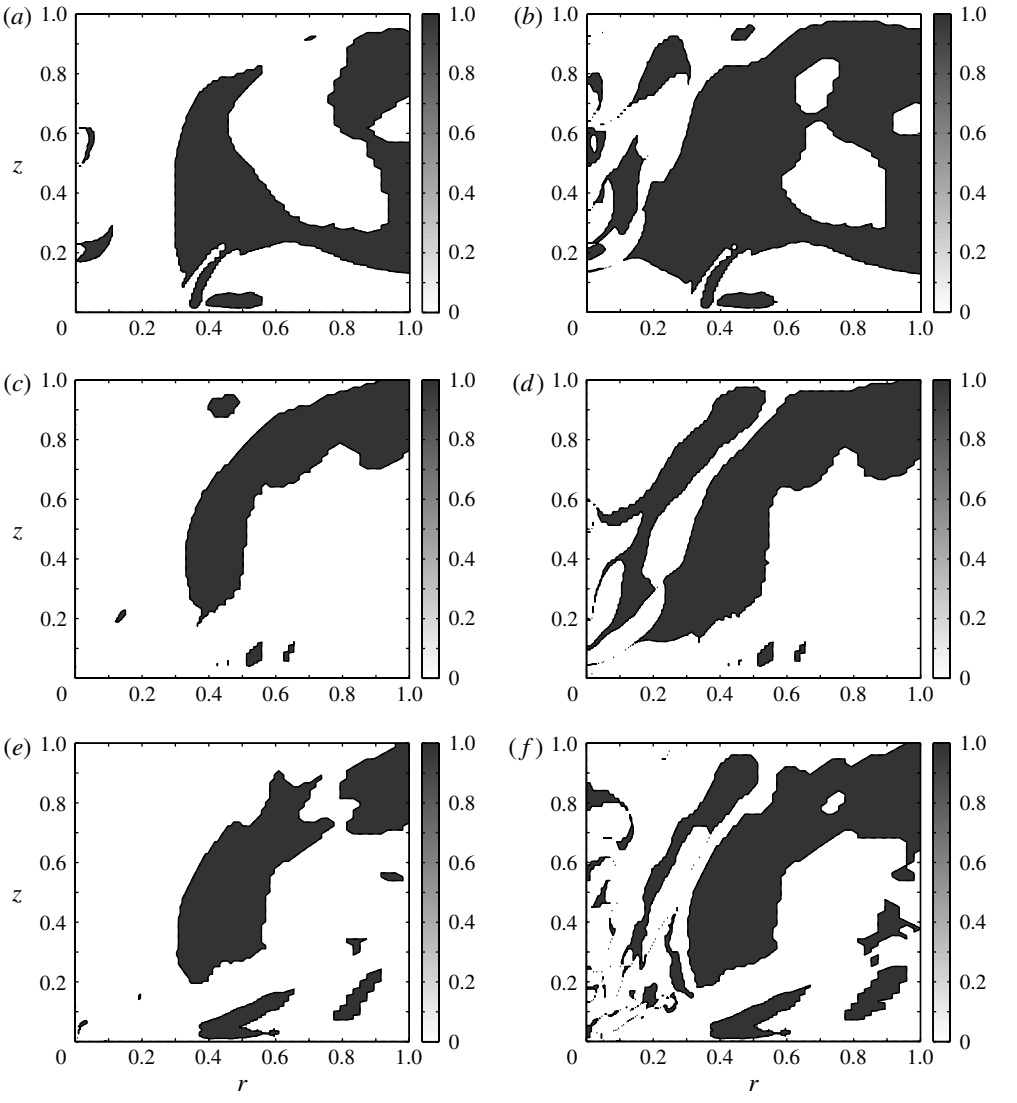

FIGURE 26. Locations in the basic-state flow for (*a,b*) the OCV, (*c,d*) DVJ, and (*e,f*) TCV that satisfy the necessary condition for axisymmetric instability of Howard & Gupta (1962) (*a,c,e*) or the sufficient condition for asymmetric instability of Leibovich & Stewartson (1983) (*b,d,f*). Shaded areas indicate the conditions are satisfied.

simulations of tornado-like vortices. Professor Fiedler, Dr R. Rotunno, and Dr Y. Moon provided helpful comments on earlier versions of this manuscript. This work was partially supported by the University of Miami.

REFERENCES

AGEE, E. M., SNOW, J. T., NICKERSON, F. S., CLARE, P. R., CHURCH, C. R. & SCHAAL, L. A. 1977 An observational study of the West Lafayatte, Indiana, tornado of 20 March 1976. *Mon. Weath. Rev.* **103**, 318–333.

BLUESTEIN, H. B., FRENCH, M. M., TANAMACHI, R. L., FRASIER, S., HARDWICK, K., JUNYET, F. & PAZMANY, A. L. 2007*a* Close-range observations of tornadoes in supercells made with a dual-polarization, X-band, mobile Doppler radar. *Mon. Weath. Rev.* **135**, 1522–1543.

BLUESTEIN, H. B., LEE, W.-C., BELL, M., WEISS, C. C. & PAZMANY, A. L. 2003 Mobile Doppler radar observations of a tornado in a supervell near Bassett. Nebraska, on 5 June 1999. Part II. Tornado-vortex structure. *Mon. Weath. Rev.* **131**, 2968–2984.

BLUESTEIN, H. B. & PAZMANY, A. L. 2000 Observations of tornadoes and other convective phenomena with a mobile, 3-mm wavelength, Doppler radar: the spring 1999 field experiment. *Bull. Am. Meteorol. Soc.* **81**, 2939–2951.

BLUESTEIN, H. B., WEISS, C. C., FRENCH, M. M., HOLTHAUS, E. M. & TANAMCHI, R. L. 2007*b* The structure of tornadoes near Attica, Kansas on 12 May 2004: High-resolution, mobile, Doppler radar observations. *Mon. Weath. Rev.* **135**, 475–506.

BLUESTEIN, H. B., WEISS, C. C. & PAZMANY, A. L. 2004 Doppler radar observations of dust devils in Texas. *Mon. Weath. Rev.* **132**, 209–224.

CHURCH, C. R. & SNOW, J. T. 1993 Laboratory models of tornadoes. In *The Tornado: Its Structure, Dynamics, Prediction, and Hazards* (ed. C. Church *et al.*). American Geophysical Union.

CHURCH, C. R., SNOW, J. T., BAKER, G. L. & AGEE, E. M. 1979 Characteristics of tornado-like vortices as a function of swirl ratio: a laboratory investigation. *J. Atmos. Sci.* **36**, 1755–1776.

DAVIES-JONES, R. P. 1973 The dependence of core radius on swirl ratio in a tornado simulator. *J. Atmos. Sci.* **30**, 1427–1430.

EMANUEL, K. A. 1984 A note on the stability of columnar vortices. *J. Fluid Mech.* **145**, 235–238.

ESCUDIER, M. P. 1984 Observations of the flow produced in a cylindrical container by a rotating end wall. *Exp. Fluids* **2**, 189–196.

FIEDLER, B. H. 1989 Conditions for laminar flow in geophysical vortices. *J. Atmos. Sci.* **46**, 252–260.

FIEDLER, B. H. 1993 Numerical simulation of axisymmetric tornado genesis in forced convection. In *The Tornado: Its Structure, Dynamics, Prediction, and Hazards* (ed. C. Church *et al.*), American Geophysical Union.

FIEDLER, B. H. 1994 The thermodynamic speed limit and its violation in axisymmetric numerical simulations of tornado-like vortices. *Atmos.-Ocean* **32**, 335–359.

FIEDLER, B. H. 1998 Wind-speed limits in numerical simulated tornadoes with suction vortices. *Q. J. Meteorol. Soc.* **124**, 2377–2392.

FIEDLER, B. H. 2009 Suction vortices and spiral breakdown in numerical simulations of tornado-like vortices. *Atmos. Sci. Lett.* **10**, 109–114.

FIEDLER, B. H. & ROTUNNO, R. 1986 A theory for the maximum windspeeds in tornado-like vortices. *J. Atmos. Sci.* **43**, 2328–2340.

FUJITA, T. T. 1970 The Lubbock tornadoes: a study of suction spots. *Weatherwise* **23**, 160–173.

GALL, R. L. 1983 A linear analysis of the multiple vortex phenomenon in simulated tornadoes. *J. Atmos. Sci.* **40**, 2010–2024.

GALL, R. L. 1985 Linear dynamics of the multiple-vortex phenomenon in tornadoes. *J. Atmos. Sci.* **42**, 761–772.

GALLARE, F. & CHOMAZ, J.-M. 2003 Mode selection in swirling jet experiments: a linear stability analysis. *J. Fluid Mech.* **494**, 223–253.

HALL, M. G. 1972 Vortex breakdown. *Annu. Rev. Fluid Mech.* **4**, 195–218.

HALL, N. M. J. & SARDESHMUKH, P. D. 1998 Is the time-mean northern hemisphere flow baroclinically unstable? *J. Atmos. Sci.* **55**, 41–56.

HOWARD, L. N. & GUPTA, A. S. 1962 On the hydrodynamic and hydromagnetic stability of swirling flows. *J. Fluid Mech.* **14**, 463–476.

HOWELLS, P. C., ROTUNNO, R. & SMITH, R. K. 1988 A comparative study of atmospheric and laboratory analogue numerical tornado-vortex models. *Q. J. R. Meteorol. Soc.* **114**, 801–822.

LEE, W.-C. & WURMAN, J. 2005 Diagnosed three-dimensional axisymmetric structure of the Mulhall tornado on 3 May 1999. *J. Atmos. Sci.* **62**, 2373–2393.

LEIBOVICH, S. 1984 Vortex stability and breakdown: survey and extension. *AIAA J.* **22**, 1192–1205.

LEIBOVICH, S. & STEWARTSON, K. 1983 A sufficient condition for the instability of columnar vortices. *J. Fluid Mech.* **126**, 335–356.

LEWELLEN, D. C. & LEWELLEN, W. S. 2007*a* Near-surface intensification of tornado vortices. *J. Atmos. Sci.* **64**, 2176–2194.

LEWELLEN, D. C. & LEWELLEN, W. S. 2007*b* Near-surface vortex intensification through corner flow collapse. *J. Atmos. Sci.* **64**, 2195–2209.

LEWELLEN, W. S., LEWELLEN, D. C. & SYKES, R. I. 1997 Large-eddy simulation of a tornado's interaction with the surface. *J. Atmos. Sci.* **54**, 581–605.

LEWELLEN, D. C., LEWELLEN, W. S. & XIA, J. 2000 The influence of a local swirl ratio on tornado intensification near the surface. *J. Atmos. Sci.* **57**, 527–544.

LILLY, D. K. 1969 Tornado dynamics. NCAR Manuscript 69-117, 39 pp. [Available from NCAR, P. O. Box 3000, Boulder, CO 80307].

LUGT, H. J. 1989 Vortex breakdown in atmospheric columnar vortices. *Bull. Am. Meteorol. Soc.* **70**, 1526–1537.

MARKOWSKI, P. & RICHARDSON, Y. 2010 *Mesoscale Meteorology in Mid-latitudes*. Wiley-Blackwell.

MAXWORTHY, T. 1973 Vorticity source for large-scale dust devils and other comments on naturally occurring vortices. *J. Atmos. Sci.* **30**, 1717–1720.

MICHAELKE, A. & TIMME, A. 1967 On the inviscid instability of certain two-dimensional vortex-type flows. *J. Fluid Mech.* **29**, 647–666.

NOLAN, D. S. 2001 The stabilizing effects of axial stretching on vortex dynamics. *Phys. Fluids* **13**, 1724–1738.

NOLAN, D. S. 2005*a* Instabilities in hurricane-like boundary layers. *Dyn. Atmos. Oceans* **40**, 209–236.

NOLAN, D. S. 2005*b* A new scaling for tornado-like vortices. *J. Atmos. Sci.* **62**, 2639–2645.

NOLAN, D. S. & FARRELL, B. F. 1999*a* Generalized stability analyses of asymmetric disturbances in one- and two-celled vortices maintained by radial inflow. *J. Atmos. Sci.* **56**, 1282–1307.

NOLAN, D. S. & FARRELL, B. F. 1999*b* The structure and dynamics of tornado-like vortices. *J. Atmos. Sci.* **56**, 2908–2936.

NOLAN, D. S. & GRASSO, L. D. 2003 Nonhydrostatic, three-dimensional perturbations to balanced, hurricane-like vortices. Part II. Symmetric response and nonlinear simulations. *J. Atmos. Sci.* **60**, 2717–2745.

NOLAN, D. S. & MONTGOMERY, M. T. 2002*a* Three-dimensional stability analyses of tornado-like vortices with secondary circulations. *Preprints, 21st Conf. on Severe Local Storms, San Antonio, TX*, pp. 477–480. Am. Meteor. Soc..

NOLAN, D. S. & MONTGOMERY, M. T. 2002*b* Nonhydrostatic, three-dimensional perturbations to balanced, hurricane-like vortices. Part I. Linearized formulation, stability, and evolution. *J. Atmos. Sci.* **59**, 2989–3020.

OBERLEITHNER, K., SIEBER, M., NAYERI, C. N., PASCHEREIT, C. O., PETZ, C., HEGE, H.-C., NOACK, B. R. & WYGNANSKI, I. 2011 Three-dimensional coherent structures in a swirling jet undergoing vortex breakdown: stability analysis and empirical mode construction. *J. Fluid Mech.* **679**, 383–414.

PAULEY, R. L. & SNOW, J. T. 1988 On the kinematics and dynamics of the 18 July 1986 Minneapolis Tornado. *Mon. Weath. Rev.* **116**, 2731–2736.

ROTUNNO, R. 1978 A note on the stability of a cylindrical vortex sheet. *J. Fluid Mech.* **87**, 761–771.

ROTUNNO, R. 1979 A study in tornado-like vortex dynamics. *J. Atmos. Sci.* **36**, 140–155.

ROTUNNO, R. 1984 An investigation of a three-dimensional asymmetric vortex. *J. Atmos. Sci.* **41**, 283–298.

SCHUBERT, W. H., MONTGOMERY, M. T., TAFT, R. K., GUINN, T. A., FULTON, S. R., KOSSIN, J. P. & EDWARDS, J. P 1999 Polygonal eyewalls, asymmetric eye contraction, and potential vorticity mixing in hurricanes. *J. Atmos. Sci.* **56**, 1197–1223.

SERRE, E. & BONTOUX, P. 2002 Vortex breakdown in a three-dimensional swirling flow. *J. Fluid Mech.* **459**, 347–370.

SHTERN, V. & HUSSAIN, F. 1999 Collapse, symmetry breaking, and hysteresis in swirling flows. *Annu. Rev. Fluid Mech.* **31**, 537–566.

SNOW, J. T. 1982 A review of recent advances in tornado vortex dynamics. *Rev. Geophys.* **20**, 953–964.

STALEY, D. O. & GALL, R. L. 1979 Barotropic instability in a tornado vortex. *J. Atmos. Sci.* **36**, 973–981.

STEFFENS, J. L. 1988 The effect of vorticity-profile shape on the instability of a two-dimensional vortex. *J. Atmos. Sci.* **45**, 254–260.

TANAMACHI, R. L., BLUESTEIN, H. B., LEE, W.-C., BELL, M. & PAZMANY, A. 2007 Ground-based velocity-track display (GBVTD) analysis of W-band Doppler radar data in a tornado near Stockton, Kansas, on 15 May 1999. *Mon. Weath. Rev.* **135**, 783–800.

TERWEY, W. D. & MONTGOMERY, M. T. 2002 Wavenumber-2 and wavenumber-m vortex Rossby wave instabilities in a generalized three-region model. *J. Atmos. Sci.* **59**, 2421–2427.

WAKIMOTO, R. M., ATKINS, N. T. & WURMAN, J. 2011 The LaGrange tornado during VORTEX2. Part I. Photogrammetric analysis of tornado combined with single-Doppler radar. *Mon. Weath. Rev.* **139**, 2233–2258.

WALKO, R. & GALL, R. 1984 A two-dimensional linear stability analysis of the multiple vortex phenomenon. *J. Atmos. Sci.* **41**, 3456–3471.

WARD, N. B. 1972 The exploration of certain features of tornado dynamics using a laboratory model. *J. Atmos. Sci.* **29**, 1194–1204.

WURMAN, J. 2002 The multiple-vortex structure of a tornado. *Wea. Forecasting* **17**, 473–505.

WURMAN, J., STRAKA, J. M. & RASMUSSEN, E. N. 1996 Fine-scale Doppler radar observations of tornadoes. *Science* **272**, 1774–1777.

ZHANG, W. & SARKAR, P. P. 2012 Near-ground tornado-like vortex structure resolved by particle image velocimetry (PIV). *Exp. Fluids* **52**, 479–493.